Scenario optimization for the tokamak ramp-down phase in RAPTOR. Part B: safe termination of DEMO plasmas

OPEN ACCESS
IOP Publishing
Plasma Physics and Controlled Fusion
Plasma Phys. Control. Fusion **66** (2024) 025007 (24pp)
https://doi.org/10.1088/1361-6587/ad157c

Scenario optimization for the tokamak ramp-down phase in RAPTOR. Part B: safe termination of DEMO plasmas

S Van Mulders[1,7,*], O Sauter[1], C Contré[1], E Fable[2], F Felici[1], P Manas[3], M Mattei[4], F Palermo[5], M Siccinio[2] and A A Teplukhina[6]

[1] Ecole Polytechnique Fédérale de Lausanne (EPFL), Swiss Plasma Center (SPC), CH-1015 Lausanne, Switzerland
[2] Max-Planck-Institut für Plasmaphysik, 85748 Garching, Germany
[3] CEA, IRFM, Saint Paul-lez-Durance, France
[4] Universitá di Napoli Federico II, Consorzio CREATE, Napoli, Italy
[5] Culham Centre for Fusion Energy, Abingdon, United Kingdom
[6] Princeton Plasma Physics Laboratory, Princeton 08543, NJ, United States of America

E-mail: simon.vanmulders@iter.org

Received 8 August 2023, revised 5 December 2023
Accepted for publication 13 December 2023
Published 27 December 2023

Abstract

An optimized plasma current ramp-down strategy is critical for safe and fast termination of plasma discharges in a tokamak demonstration fusion reactor (DEMO), both in planned and emergency scenarios, avoiding plasma disruptions and excessive heat loads to the first wall. Plasma stability limits and machine-specific technical requirements constrain the stable envelope through which the plasma must be navigated. Large amounts of auxiliary heating are required throughout the ramp-down phase, to avoid a radiative collapse in the presence of intrinsic tungsten and seeded xenon impurities, as quantitatively estimated in this work. As the plasma current is reduced, the current density becomes increasingly peaked, reflected by a growing value of the internal inductance ℓ_{i3}, resulting in reduced controllability of the vertical position of the plasma. The feasibility of different plasma current ramp-down rates is tested by applying an automated optimization framework embedding the RAPTOR core transport solver. Optimal time traces for plasma current $I_p(t)$ and plasma elongation $\kappa(t)$ are proposed, to satisfy an I_p-dependent upper limit on the plasma internal inductance, as obtained from vertical stability studies using the CREATE-NL code, as well as a constraint on the time evolution of q_{95}, to avoid an ideal MHD mode. A negative current density near the plasma edge is observed in our simulations, even for the most conservative I_p ramp-down rate, indicating significant transient dynamics due to a large resistive time.

Keywords: DEMO, RAPTOR, tokamak scenario development, tokamak transport, integrated tokamak simulation, ramp-down optimization

[7] Present address: ITER Organization, Route de Vinon sur Verdon, St Paul Lez Durance 13115, France.
[*] Author to whom any correspondence should be addressed.

1. Introduction

Safe termination of a burning plasma in a DEMO reactor is a highly non-trivial task. The high energy content of a reactor-grade plasma and the limited thickness of a reactor first wall (to allow for sufficient tritium breeding), lead to a very small tolerance for plasma disruption events. As safe termination scenarios, both for routine and for emergency shutdown, are critical to any viable tokamak reactor concept, present-day tokamak experiments have started to investigate stable ramp-down solutions, guided by modeling tools.

Modeling and optimization with the RAPTOR code, applied to TCV, ASDEX Upgrade (AUG) and JET, has allowed to increase the plasma current ramp-down rate while maintaining the plasma radially and vertically stable, by optimizing the time evolution of plasma current and elongation throughout the ramp-down phase [1]. On DIII-D, vertical displacement events (VDEs) could be successfully prevented by adjusting the plasma elongation and the inner-gap to the vessel wall, in response to real-time estimators of the proximity to the vertical stability limit [2]. Furthermore, [2] presents the analysis of a large data set of emergency shutdowns after large tearing modes. Modeling of the ramp-down phase for AUG is discussed in [3, 4] and for JET in [5–7].

Fast simulators like RAPTOR allow to systematically explore reactor operating points and scenario dynamics, and to automatize the search for optimal control strategies. In [8], METIS [9] is used to explore operating points for a pulsed and a steady state DEMO design. Note that the large size and the high temperature of a DEMO plasma core lead to a very slow diffusion time scale of the current density. This clearly illustrates the need for a fast simulation tool to optimize a DEMO scenario.

While we focus on ramp-down optimization for a DEMO plasma, similar considerations are relevant for ITER. Time-dependent, self-consistent ramp-down simulations are needed to project how observations on present-day devices will scale to ITER operation, due to non-linear dynamics and the varying characteristic time scales at play, as argued in [10]. The complexity of this task, requiring simultaneous accounting for plasma position and shape control, energy and density evolution, MHD mode activity and impurity transport, demands an analysis that combines a range of time-dependent equilibrium and transport solvers of varying fidelity. The increase of internal inductance after the HL transition and the need for a significant elongation reduction during ramp-down, resulting in an ITER termination scenario remaining at relatively low $q_{95} \sim 3$ have been discussed in [11]. Furthermore, [11] makes the observation that I_p will be an effective control parameter for the internal inductance evolution, as the ITER ramp-down is fast with respect to the resistive time τ_R. Strategies for pellet fueling and auxiliary heating to avoid tungsten accumulation during the ITER baseline ramp-down have been studied in [7, 12].

In the previous paper, 'Part A: Analysis and model validation on ASDEX Upgrade' [13], we have discussed how RAPTOR has been applied to model AUG ramp-down scenarios, including the impact of plasma current, auxiliary heating and shaping. Successful validation on present-day machines increases confidence that the same models, coupled to conservative assumptions regarding heat and particle transport, can be used to study optimized ramp-down strategies for DEMO.

2. Challenges for DEMO ramp-down scenarios

Even though the European DEMO strategy aims to maximize its reliance on a conservative physics basis that can be explored on ITER, some fundamentally new challenges will arise.

- Seeded impurities like xenon are required to radiate sufficient heat from the plasma core, maintaining the heat load to the divertor tiles manageable (even in the presence of detachment). Depending on the plasma temperature, the plasma can (locally) be in a regime where a decrease in T_e leads to an increase in radiated power (from both Xe and W [14, 15]), triggering a radiative collapse of the plasma. In the DEMO power balance, both the main source term (fusion power) and the main sink term (impurity radiation) are non-linearly dependent on the plasma temperature and density, making the plasma largely self-regulated. Thus, the dynamics of a burning plasma with high radiation fraction is highly non-linear, while external actuators are less effective with respect to present-day machines.
- To maintain the integrity of the thin metal wall (which must be thinner compared to ITER to allow for tritium breeding [16]), a loss of plasma control at high plasma current $I_p >\sim$ 5MA and high stored energy is unacceptable. Developing a reliable ramp-down strategy, both for planned and emergency termination of the plasma, is hence critical for the DEMO mission.

An emergency shutdown scenario in the event of divertor reattachment is discussed in [14]. Divertor sweeping is proposed to delay the heat flux to the coolant becoming critical. While maintaining this emergency measure, temporarily averting target plate damage [17], a fast plasma current ramp-down is paramount. Furthermore, a fast reduction of plasma current is beneficial to reduce the forces experienced by the vacuum vessel in case of a disruption, which are proportional to I_p^2. However, note that for non-emergency ramp-up and ramp-down scenarios, slower ramp phases with a slow density evolution might be preferred to allow the turbine to follow slow changes in fusion power, to maximize exploitation for electric energy production [14, 18].

In this paper, the feasibility of different plasma current ramp-down rates is investigated. Through action of the central solenoid, the loop voltage at the edge of the plasma is controlled to maintain the imposed I_p time evolution. The reduced loop voltage at the edge then provides a driving force for outward current diffusion. However, due to the high temperatures and the large size of a DEMO plasma, current diffusion is extremely slow. A fast current ramp-down will hence tend

to peak the current density profile, or equivalently, increase the plasma internal inductance ℓ_{i3}, resulting in reduced controllability of the vertical position of the plasma. Since a loss of position control of the plasma column needs to be avoided throughout the entire ramp-down, the minimum time window required to safely terminate the discharge is constrained by the *vertical stability limit*. For the work presented in this paper, CREATE-NL simulations [19] of the vertical position stabilization control loop for DEMO [20] are used to obtain the upper limit for the internal inductance.

Note that vertical stabilization of the plasma column is projected to become more challenging for future tokamak reactors with respect to present-day devices. Future tokamaks like DEMO aim to maximize performance by significantly elongating the plasma. Compared to present devices, the current diffusion time scale is very long, while conductive walls are further away from the plasma due to the presence of tritium breeding blankets. Furthermore, measurements are complicated by the presence of 14.1 MeV neutrons and control will be less efficient due to the difficulty of putting internal coils inside the vessel and the comparatively long distance to the poloidal field coils (which are located outside of the toroidal field coils [21]).

In addition to the vertical stability limit, a set of further constraints limits the operation space of feasible ramp-downs.

- In order to ensure stable *radial position control*, the maximum rates of change of poloidal field coil currents impose an upper limit on the time derivative of the vertical magnetic field B_v, which can be written as:

$$B_v = \frac{\mu_0 I_p}{4\pi R}\left(\ln\left(\frac{8R}{a\kappa^{0.5}}\right) + \beta_p + 0.5\ell_{i3} - 1.5\right). \quad (1)$$

  Rapid changes of any of the parameters in equation (1), e.g. during the HL transition, can hence potentially cause a loss of radial position control.
- Since the *Greenwald density limit* [22], the upper limit on the plasma (edge) density [23, 24], is proportional to the plasma current, the density has to be decreased throughout the ramp-down phase. In the present work, we assume that a constant Greenwald fraction can be maintained during the H-mode and L-mode phases. In practice, the particle confinement time and pumping capacity limit the maximum achievable density decay rate. On present-day devices, maintaining regular ELMs during the ramp-down H-mode phase is observed to be critical in order to avoid an increase in Greenwald fraction [11, 25].
- While terminating a burning plasma, the fusion power is reduced, by changing the isotope DT concentration and by bringing down the density ($P_{fus} \sim n_e^2$). The presence of the inherent W impurity and the seeded Xe impurity to boost core radiation make the plasma prone to a *radiative collapse*: while the alpha heating drops, the average cooling factor of W and Xe increases for decreasing T_e. Methods for the removal of Xe and W or large auxiliary heating power resources are required to maintain a positive power balance throughout the entire ramp-down phase.

Both the vertical and the radial position control problem illustrate the impact of the time evolution of internal plasma profiles on the magnetic control, through parameters like ℓ_{i3} and β_{pol}. Conversely, the plasma shape evolution can be used as an actuator to drive changes to the plasma profile evolution: in [1], it was found that a fast decrease in plasma elongation allows to limit the increase of the internal inductance (while simultaneously widening the margin for vertical controllability). Furthermore, the plasma shape impacts the thermal confinement quality of the plasma. These examples illustrate the inherently coupled nature of the kinetic (q, T_e, n_e) and magnetic (position and shape) control problems. The constraints mentioned in this section, non-linearly dependent on the plasma state itself, have to be simultaneously met. A fast transport solver like RAPTOR captures some of these non-linearities and can hence assist in the design process of safe ramp-down strategies, as will be presented in the remainder of this paper.

The set-up of the RAPTOR simulations is described in section 3, highlighting the various non-linearities captured by the model. In section 4, a stationary operating point for a DEMO reactor is established, which will serve as the initial state for the ramp-down simulations. The time traces of auxiliary heating and Xe impurity concentration are manually optimized to find a feasible ramp-down scenario, avoiding a radiative collapse, in section 5. The upper limit for the internal inductance, obtained from CREATE-NL vertical stability calculations, is introduced in section 6. For various ramp-down rates, L-mode confinement quality assumptions and HL transition timings, the feasibility with respect to vertical and radial position control is assessed. Optimization with respect to vertical stability is studied in section 7. The RAPTOR non-linear optimization algorithms are used to optimize the ramp-down time traces of plasma current and elongation to ensure operation within the vertically stable operating envelope extracted from CREATE-NL calculations, while avoiding decreasing values of q_{95} that could compromise MHD stability. The main insights resulting from our ramp-down simulations are summarized in section 8. Conclusions are formulated in section 9.

3. Simulation set-up for DEMO simulations

The termination simulations in this paper cover a plasma current ramp from $I_{p\ \text{flat top}} = 17.75\text{MA}$ down to $I_{p\ \text{final}} = 5.00\text{MA}$. Depending on the I_p ramp-down rate, different simulation time windows result, with $t_{\text{final}} = \frac{I_{p\ \text{final}} - I_{p\ \text{flat top}}}{dI_p/dt}$ ($t_0 = 0$ s at the end of flat-top).

3.1. Stationary state (initial state ramp-down)

To obtain a stationary solution, describing the plasma profiles by the end of the flat-top phase, the RAPTOR stationary state solver, described in [26], is used. The obtained stationary state, with a radially flat loop voltage profile $U_{pl}(\rho)$, is used as the initial state x_0 for the ramp-down simulations.

3.2. Transport equations and heat sources

- The transport equations solved for are electron heat transport $T_e(\rho,t)$, electron density transport $n_e(\rho,t)$ and poloidal flux diffusion $\psi(\rho,t)$ (equivalent to current diffusion). These equations are evolved from $t_0 = 0$ s to t_{final} on the full radial domain $\rho \in [0\ 1]$. The boundary conditions for T_e and n_e at $\rho = 1$ are set to respectively 200 eV and 0.5×10^{19} m^{-3}.[8] The temperature for the ion species is set equal to the electron temperature, which is justified by the assumption that equipartitioning occurs on a fast time scale as compared to the large confinement time expected for DEMO.
- For the main ions, a 50/50 deuterium/tritium fuel mix is assumed. A set of three impurities is assumed, as discussed later, with an impurity density set proportional to n_e, with a user-defined, time-dependent factor. $n_D + n_T$ and Z_{eff} are solved for by imposing quasi-neutrality and evaluating the effective charge equation for Z_{eff}.
- The flat-top neutral beam deposition profiles $p_{nbi,e}$ and j_{nbi} are taken from a METIS [9] DEMO simulation, with a time-dependent factor scaling the profiles to match the requested total power evolution $P_{nbi}(t)$. The time trace of this factor is calculated before the RAPTOR simulation, taking into account the programmed plasma volume evolution. Note that while the total injected power is reduced during ramp-down, the deposition profile is maintained self-similar throughout the simulation. Updating the NBI source profiles, self-consistently with the changing plasma density and equilibrium, e.g. through direct coupling with the RABBIT code [27], is left for future work.
- The EC heating is deposited in the center $\rho_{\text{dep}} = 0$ with $w_{\text{dep}} = 0.1$, without any current drive.
- The fueling of the plasma is modeled indirectly: while the electron diffusion coefficient is set in relation to the electron heat diffusivity $D_e = 0.2\chi_e$, the density gradient in the edge region of the plasma evolves in response to a dedicated term in the formula for the electron pinch velocity (see the term including μ_{n_e} in equation 2 in the Part A paper [13]). The trace of the edge density gradient is feedback controlled to track the desired time evolution for the line average density, as described in more detail in section 3.3.
- The alpha power density is evaluated with the formula described in [28], consistently calculating the electron and ion heating contributions, according to the formula derived in [29]. Since this alpha power model is relatively simplistic (not taking into account fast ion losses due to orbit and ripple effects and diffusion across the plasma during the slowing down time), a multiplicative factor $c_\alpha = 0.73$ was introduced to obtain the DEMO RAPTOR simulations reported in [30], benchmarked against more complete ASTRA simulations.

[8] Note that in the present work, these boundary conditions have not been varied. Self-consistent modeling of the separatrix conditions, its implications on detachment control, and the pedestal, including an improved estimate of the pedestal-driven bootstrap current, are left for future work.

- The transition from H-mode to L-mode confinement is modeled by a gradual ramp (during the HL transition interval) of parameters in the analytical transport coefficient formulas for the T_e and the n_e equation (equations (1) and (2) in the Part A paper [13]). As explained in the following section 3.3, dedicated parameters enable the modification of core and edge gradients, corresponding to the confinement quality degradation and the change in core logarithmic gradients characteristic to the HL transition.

3.3. Heat and density gradient-based transport model

The present paper applies the same gradient-based transport model that has been applied for AUG ramp-down modeling in the Part A paper [13]. We repeat here the main assumptions underlying the tranport model, as well as those settings that are specific to the application for DEMO. For more details regarding the analytical formulas for heat and particle diffusivities, we refer the reader to section 2.1 of the Part A paper [13].

The gradient-based model assumes the formation of three radially separated regions:

(i) a central region $\rho < \rho_{\text{inv}} (= \rho_{q=1})$ with high transport, to mimic the profile flattening caused by sawteeth or other transport-enhancing phenomena (in the absence of a $q = 1$ surface, we put $\rho_{\text{inv}} = 0.1$, as flattened profiles toward the magnetic axis can occur even in the absence of sawtooth activity, e.g. in the presence of kinetic ballooning modes [31]);
(ii) an intermediate stiff core region characterized by constant logarithmic gradients $\lambda_{T_e} = -\frac{d\log T_e}{d\rho}$ and $\lambda_{n_e} = -\frac{d\log n_e}{d\rho}$;
(iii) a pedestal region with linear gradients $\mu_{T_e} = -\frac{dT_e}{d\rho}$ and $\mu_{n_e} = -\frac{dn_e}{d\rho}$.

For the DEMO ramp-down simulations in the present paper, we use the gradient-based transport model because its prediction is well-defined, based on the $H_{98,y2}$ confinement factor ($H_{98,y2} = 1$ is assumed here in H-mode, allowing for a conservative prediction), and it models across the whole plasma radius for both L- and H-mode plasmas. The LH transition is modeled through the user-defined time trace of the confinement factor and the resulting modifications of the transport coefficients. The values used for the logarithmic gradients λ_{T_e,n_e} are inspired by the available literature on predictive DEMO modeling, as described later in this paper.

The time traces $\mu_{T_e,n_e}(t)$, governing the pedestal confinement quality, are set as the sum of a feedforward and a feedback contribution. The feedforward contribution provides an initial estimate of the time evolution of the pedestal gradient. The feedback controller, with a proportional and an integral term, adds a corrective term to bring the plasma confinement time and line-averaged density towards pre-defined reference traces $\tau_E \sim H_{\text{ref}}\tau_{E\ scl}$ and $n_{el} \sim n_{el\ \text{ref}}$, making use of the error terms defined in equation (2). More technical details on application of the gradient-based transport model can be found in section 5.2.4 of [32]

$$\mu_X(t) = \mu_X^{ff}(t) + g_p e(t) + g_i \int e(t)\,dt \text{ with}$$
$$\begin{cases} e(t) = H_{\text{ref}} - \tau_E/\tau_{E\ scl} \text{ for } X = T_e \\ e(t) = n_{el\ \text{ref}} - n_{el} \text{ for } X = n_e \end{cases} . \quad (2)$$

In the present work, the line-averaged density reference $n_{el\ \text{ref}}$ is set proportional to the Greenwald density $n_{e,Gw} = I_p/(\pi a^2)$, with a user-defined factor $f_{Gw} = n_{el\ \text{ref}}/n_{e,Gw}$ that can be time-dependent. Different confinement time scaling $\tau_{E\ scl}$ could be applied; in this study the IPB98(y, 2) scaling law is used [33].

Note that the gradient-based transport model omits the need to provide a boundary condition at the pedestal top. This approach differs from the RAPTOR simulations for ITER in [26], where pedestal pressure values consistent with the EPED1-SOLPS fit reported in [34] were chosen, and from the RAPTOR simulations for AUG in [35], where pedestal pressure values were calculated with a scaling law derived based on previous experiments. In [13], the gradient-based transport model, with global constraints on the confinement scaling factor and the line-averaged density, has been successfully applied to model ASDEX Upgrade ramp-downs.

It is important to note that the IPB98(y, 2) scaling law is derived based on the data available on present-day machines, with modest levels of radiated power from the core plasma compared to a DEMO plasma. This raises the question how radiated power should be correctly accounted for in the calculation of confinement time and in the evaluation of the scaling law. In this paper, the confinement factor is calculated without subtracting the power radiated in the core. In appendix, simulations are presented to quantify the change of expected electron temperature profile and stored energy when the subtraction of core radiated power is included.

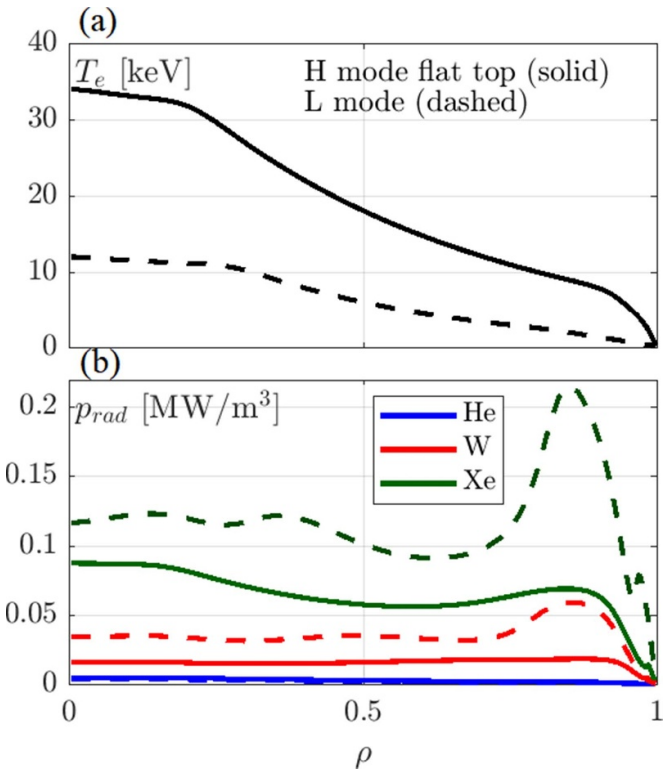

Figure 1. Radiated power from three impurities, for concentrations $n_{He}/n_e = 0.05$, $n_W/n_e = 3\ 10^{-5}$, $n_{Xe}/n_e = 5\ 10^{-4}$, as evaluated with ADAS cooling factor data, with respectively the end of flat-top T_e profile (solid lines) and a L-mode T_e profile (dashed lines). Xenon, the seeded core impurity, is the dominant radiator. Note how the HL transition during the ramp-down leads to a significant increase in radiated power, from both W and Xe. A combination of plasma heating and Xe removal is required to avoid a radiative collapse, as studied later in this paper. (a) $T_e(\rho)$; (b) $p_{\text{rad}}(\rho)$.

3.4. Impurity concentrations and line radiation

Three impurity species are considered:

(i) an intrinsic tungsten influx is assumed since W is envisioned as plasma-facing component armour material,
(ii) xenon is seeded in the core to enhance the radiated power, limiting the divertor heat load,
(iii) as alpha particles born from fusion reactions thermalise, heating the plasma, they constitute a source of helium impurities.

At present, RAPTOR does not solve for impurity transport[9]. Within the simulation, the radial distribution of the impurities is taken proportionally to the electron density n_e, with a user-defined time-dependent concentration factor (the resulting time evolution of Z_{eff} is calculated self-consistently).

[9] Note that the lack of impurity transport is an important limitation for ramp-down studies, as avoiding a radiative collapse caused by impurity accumulation poses an important constraint. The impurity concetration profiles and time evolution imposed in RAPTOR should be verified by higher fidelity integrated modeling codes. Alternatively, reduced analytical models [36] for (heavy) impurity transport could be integrated in the code.

Impurity radiation of the three impurity species is evaluated with the formula equation (3), with $L_{\text{imp}}(T_e)$ the impurity cooling factor taken from the ADAS database [15, 37, 38]

$$P_{\text{rad}} = n_e n_{\text{imp}} L_{\text{imp}}(T_e) . \quad (3)$$

Note that impurities affect the plasma power balance both by dilution of the main ions, impacting the fusion power, and by the emitted line radiation. The second process is highly non-linear with respect to temperature since the average cooling factor increases throughout the plasma core for decreasing T_e (as illustrated in figure 1). Under the modeling assumption $T_i/T_e = 1$, the fusion power, and the alpha self-heating of the plasma, will decrease simultaneously. This dynamical process clearly has the potential of triggering a runaway process, with increased radiation and decreased fusion power further decreasing T_e. Note that a deviation of $T_i/T_e = 1$ during ramp-down would impact the remaining alpha power, directly influencing the heat balance and margin to radiative collapse.

3.5. Equilibrium geometry

The equilibrium geometry used for the RAPTOR simulations is based on the free boundary equilibrium calculations in

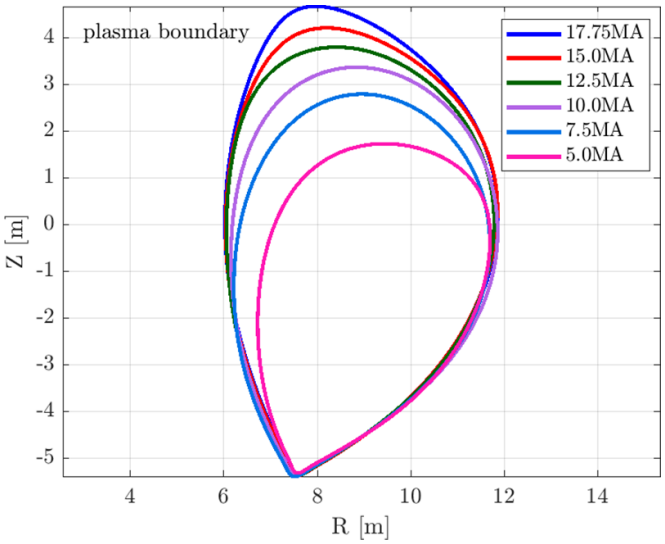

Figure 2. Plasma boundary shapes at different values of the plasma current during the ramp-down phase, simulated with the free boundary equilibrium solver CREATE-NL [19], as reported in [20]. The equilibrium geometry of these equilibria is used for the RAPTOR simulations in this paper.

CREATE-NL. The plasma boundary shapes at different times in the plasma ramp-down, at different values of the plasma current, are shown in figure 2. The geometry metrics corresponding to these equilibria are assigned to the time in the RAPTOR simulation when the corresponding plasma current is reached. For intermediate times, the geometry metrics are interpolated linearly. The CREATE-NL calculations have also been used to obtain an operating envelope for vertically stable operation during the DEMO ramp-down phase, as explained in section 6.2.

The equilibria have a lower single null configuration. The elongation is reduced during the ramp-down, while the last closed flux surface (LCFS) shape close to the X-point remains mostly unchanged, easing the heat exhaust challenge for the divertor by maintaining the magnetic geometry in the strike points region.

Note that the RAPTOR diffusion equations, as reported in [39], allow to consistently include the impact of the time derivative $\dot{\Phi}_b$ (toroidal flux enclosed by the LCFS). Results in the present paper are slightly different from what we reported in [32], since the $\dot{\Phi}_b$ term has been included in the present work and can have significant effects on current density peaking when the shape is modified relatively fast.

4. Stationary DEMO operating point

The stationary operating point established here is mainly based on considerations reported in [8, 14, 40]. The operating parameters are summarized in table 1. A central feature of a burning DEMO plasma is the high degree of self-regulation of the plasma profiles: the power balance is dominated by the plasma self-heating by the fusion-born alpha fast particles, dependent on $T_i(\rho)$, $n_{D,T}(\rho)$ and fuel dilution, and the radiated power from heavy impurities, both intrinsic (W) and seeded (Xe), with a non-linear dependence on T_e. Reliance on auxiliary current drive to tailor the q profile is minimized to maintain a high fusion gain Q.

Table 1. Operating parameters for stationary (flat loop voltage profile $U_{pl}(\rho)$) flat-top burning plasma DEMO operating point, as evaluated by RAPTOR.

Plasma current I_p	17.75 MA
On-axis tor. magnetic field B_0	5.86 T
Minor radius a	2.93 m
Major radius R_0	8.95 m
Plasma volume V	2318 m^3
Elongation κ	1.67
Triangularity δ	0.37
Bootstrap current fraction I_{bs}/I_p	0.46
Non-inductive current fraction I_{ni}/I_p	0.57
Fusion power P_{fus}	1732 MW
NBI power P_{nb}	50 MW
EC power P_{ec}	50 MW
Radiated power (fraction) P_{rad}; $f_{rad} = P_{rad}/P_{heat\ tot}$	242 MW; 54%
Separatrix power P_{sep}	205 MW
LH threshold power P_{LH}	121 MW
Plasma thermal energy $W_{th\ tot}$	1279 MJ
T_{i0}, $T_i(\rho = 0.8)$	38.1 keV, 7.9 keV
T_{e0}, $T_e(\rho = 0.8)$	38.1 keV, 7.9 keV
q_{95}	4.26
$q_{\min}$	1.05
$\langle n_e \rangle_{\text{line}}/n_{e\ Gw}$	$7.9 \times 10^{19}\,m^{-3}/6.6 \times 10^{19}\,m^{-3} = 1.20$
$n_{e0}/\langle n_e \rangle_{\text{vol}}$	$10.3 \times 10^{19}\,m^{-3}/7.1 \times 10^{19}\,m^{-3} = 1.45$
$H_{y2,98}$	1.00
β_N	2.57
Internal inductance ℓ_{i3}	0.64
Loop voltage U_{pl}	22.5 mV
Fusion power gain Q	17.3
$\langle Z_{\text{eff}} \rangle_{\text{vol}}$	2.32
n_{helium}/n_e	0.05
n_{xenon}/n_e	5×10^{-4}
n_{tungsten}/n_e	3×10^{-5}
P_{sep}/R_0	22.9 MW m^{-1}

- In [8], the physics-based transport model TGLF is used to predict critical temperature and density gradients. Based on those values, we set $\lambda_{T_e} = 2$ ($R/L_{T_e} \sim 6$) and $\lambda_{n_e} = 0.67$ ($R/L_{n_e} \sim 2$). In the L-mode phase, discussed in the next section, we assume $\lambda_{T_e\ L\ \text{mode}} = (3/2.3)\lambda_{T_e\ H\ \text{mode}}$ and $\lambda_{n_e\ L\ \text{mode}} = (1/0.5)\lambda_{n_e\ H\ \text{mode}}$, applying the same factors $\lambda_{T_e,n_e\ L\ \text{mode}}/\lambda_{T_e,n_e\ H\ \text{mode}}$ as were obtained for JET and AUG in [1]. The ion temperature is set $T_i = T_e$. Even though electron heating is dominant for the simulated DEMO plasma, $T_e \sim T_i$ is assumed due to the high confinement time scale with respect to the equipartition time scale in a DEMO device [41, 42].
- The W concentration is set to 3 10^{-5}, like in [8]. The Xe concentration is set to 5 10^{-4}, allowing for a total radiated

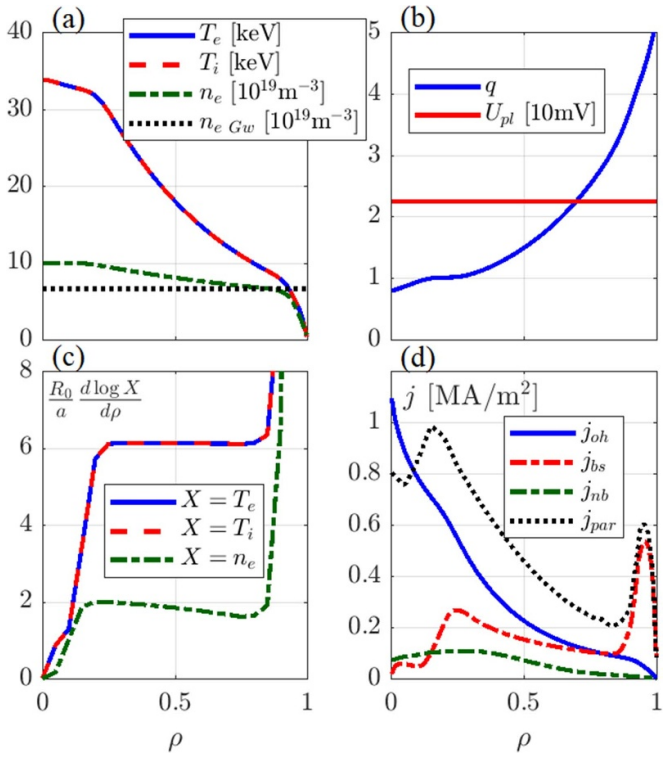

Figure 3. Radial profiles for stationary (flat loop voltage profile) flat-top burning plasma DEMO operating point, as evaluated by RAPTOR. (a) $T_e(\rho)$, $T_i(\rho)$ and $n_e(\rho)$ (with $n_{e\ Gw}$ for comparison); (b) $q(\rho)$ and $U_{pl}(\rho)$; (c) $(R_0/a)d\log T_e(\rho)/d\rho$, $(R_0/a)d\log T_i(\rho)/d\rho$ and $(R_0/a)d\log n_e(\rho)/d\rho$; (d) $j_{oh}(\rho)$, $j_{bs}(\rho)$, $j_{nb}(\rho)$ and $j_{par}(\rho)$.

power of 242 MW, which is about 54% of the total heating power. This allows to limit P_{sep}/R_0 to 22.9 MW m^{-1} (close to $P_{sep}/R_0 = 18.9$ MW m^{-1} in the EU-DEMO 2018 design point reported in [14]), while a margin $P_{sep} - P_{LH} \sim 80$ MW is maintained, to achieve good confinement and avoid any unwanted HL back transition. The helium concentration is set to 0.05, inspired by the COREDIV [43] simulation results in [8], and below the maximum He concentration of 0.075 mentioned in [30].

- The fusion power is $P_{\text{fus}} = 1732$ MW, below the 2 GW of the EU-DEMO 2018 design point. Note that this value is sensitive to assumptions regarding temperature and density peaking (higher reactivity in the center), Greenwald fraction, $H_{98y,2}$ factor and impurity concentrations (diluting the DT fuel). The impurity concentrations will also impact the discharge duration through the impact of Z_{eff} on the neoclassical conductivity, and hence on the loop voltage to be provided by the central solenoid to sustain the required ohmic plasma current.
- For the applied R/L_{n_e}, a density peaking $n_{e0}/\langle n_e\rangle_{\text{vol}} = 1.45$ results, close to what has been reported in [42]. With this density peaking a Greenwald fraction $\langle n_e\rangle_{\text{line}}/n_{e\ Gw} = 1.2$ can be achieved, while maintaining the pedestal density about 5% below the Greenwald density (the density constraint is assumed to be active at the pedestal top location [40]).
- It is interesting to note that RAPTOR predicts that bootstrap current is about half of the total plasma current. As illustrated in figure 3, the bootstrap current density is a significant source of off-axis current density (with a notable peak in the pedestal region). As a consequence, $q_{\min}$ is relatively close to unity, with a region of low magnetic shear extending to $\rho \sim 0.25$.

5. Ramp-down simulation with optimized heating power: discussion of actuators and constraints

In this section, we explore manually optimized time traces of auxiliary heating and the Xe impurity concentration, aiming for a feasible ramp-down scenario, avoiding a radiative collapse. Optimization with respect to vertical stability is presently not considered, but will be addressed in section 7.

The plasma current is reduced with a constant ramp rate $dI_p/dt = -100$ kA s^{-1}. A time trace of the evolution of $H_{98,y2}$ is pre-defined, setting both the timing of the HL transition and assumptions regarding the confinement quality during H- and L-mode. For the simulation presented in this section, the HL transition is initialized at $t = 0.2t_{final}$. The H factor transitions linearly from $H_{98y,2} = 1$ to $H_{98y,2} = 0.5$, over a duration[10] $\Delta t_{duration\ HL} = 15$ s. Note that these choices are relatively arbitrary at this stage. In the next section we will however perform a sensitivity study, changing the HL timing and

[10] The duration of the transition phase depends on the characteristic time required to decrease the pedestal and depends on a variety of plasma parameters. In [1], $\Delta t_{duration\ HL} = 0.1$ s, 0.5 s and 1 s have been derived, based on Thomson and H_α measurements, for respectively TCV, AUG and JET.

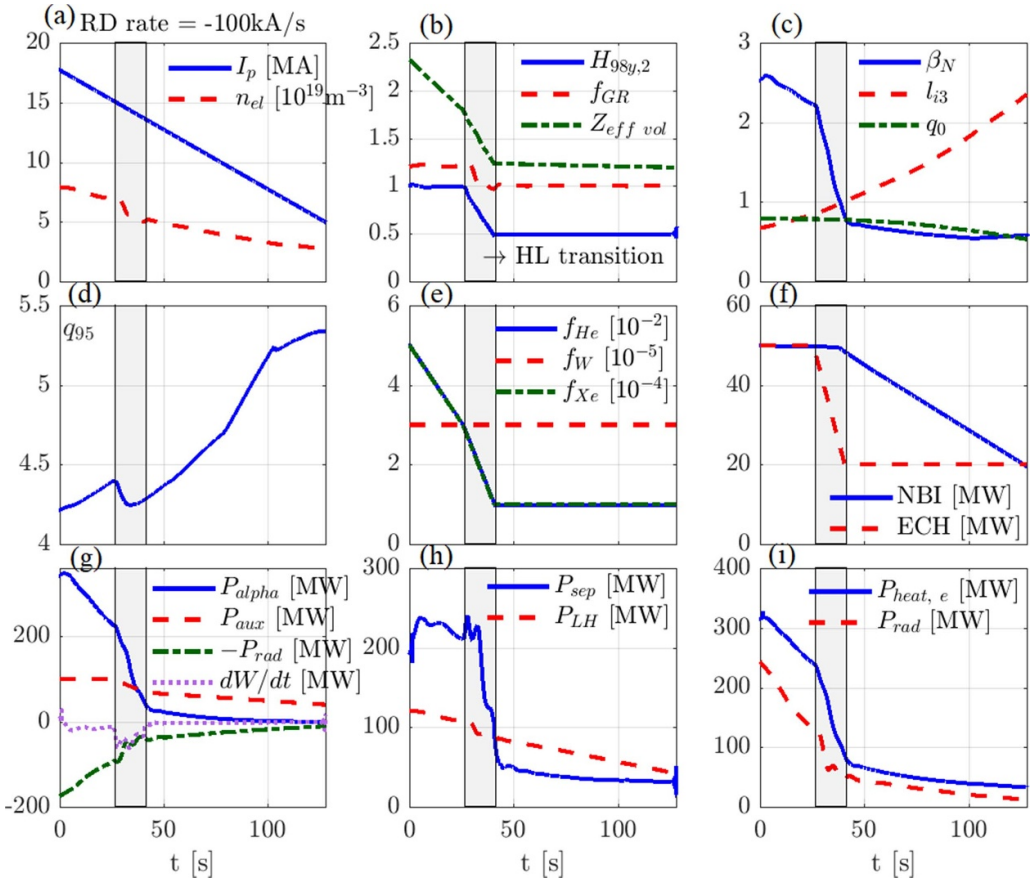

Figure 4. Key time traces for DEMO ramp-down RAPTOR simulation with $dI_p/dt = -100\,\mathrm{kA\,s^{-1}}$, $t_{HL} = 0.2t_{final}$, $H_{98y,2} = 1$ in H-mode, $H_{98y,2} = 0.5$ in L-mode. The time evolution of auxiliary heating and Xe concentration are optimized to avoid a radiative collapse. The grey box indicates the HL transition time window. (a) $I_p(t)$, $n_{el}(t)$; (b) $H_{98y,2}(t)$, $f_{Gr}(t)$ and volume average effective charge $Z_{eff\ vol}$; (c) $\beta_N(t)$, $\ell_{i3}(t)$ and $q_0(t)$; (d) $q_{95}(t)$; (e) helium concentration $f_{He}(t)$, tungsten concentration $f_W(t)$ and xenon concentration $f_{Xe}(t)$; (f) $P_{nbi}(t)$ and $P_{ec}(t)$; (g) $P_{alpha}(t)$, $P_{aux}(t)$, total radiated power $-P_{rad}(t)$ and $dW(t)/dt$; (h) $P_{sep}(t)$ and $P_{LH}(t)$; (i) $P_{heat,\ e}$ and total radiated power $P_{rad}(t)$.

L-mode confinement factor. An overview of the evolution of various parameters during the ramp-down simulation is given in figure 4.

5.1. Power balance and impurity concentrations

We list some of the constraints and considerations that have been taken into account when designing these ramp-down traces.

5.1.1. Significant auxiliary heating required throughout the entire ramp-down phase. Even if the Xe concentration can be efficiently reduced during the ramp-down, significant auxiliary heating of the plasma throughout the entire modeled ramp-down phase (i.e. the diverted phase down to $I_p = 5\,\mathrm{MA}$) is mandatory to avoid a radiative collapse. This is due to the combined effect of an increasing cooling factor for W and Xe for reducing T_e, and a simultaneous sharp decrease of the alpha power for reducing T_i and n_e (the density has to be reduced simultaneously with the plasma current to avoid an increasing violation of the Greenwald density limit). Note that higher fidelity simulations are required to assess the feasibility of the proposed ramp-down rates of density and Xe impurity concentration, taking into account the expected particle confinement time (usually the particle confinement time is 5-10 times larger compared to the energy confinement time [44]), impurity confinement time and pump efficiency.

To conclude: the plasma needs significant auxiliary heating while being terminated ($P_{ec} = 50\,\mathrm{MW} + P_{nb} = 50\,\mathrm{MW}$ at the beginning of ramp-down, maintaining $P_{ec} = 20\,\mathrm{MW} + P_{nb} = 20\,\mathrm{MW}$ by $t = t_{final}$, when $I_p = 5\,\mathrm{MA}$). The margin with respect to radiative instability can be evaluated from the bottom right plot in figure 4: the heating power to the electrons $P_{heat\ e}$ should be maintained above the radiated power P_{rad}, throughout the ramp-down. The margin is relatively small at the end of the HL transition: with $P_{aux} \sim 70\,\mathrm{MW}$, a margin $P_{heat\ e} - P_{rad} \sim 20\,\mathrm{MW}$ can be maintained. Note that the heating of discharges with high radiation during ramp-down is already common practice on present-day devices, as discussed for AUG in the Part A paper [13]. Evolution of the shine-through power during ramp-down and compatibility with first wall head load limits should be assessed with dedicated simulations.

5.1.2. Self-consistent triggering of HL transition. While enough heating power needs to be maintained throughout the L-mode phase of the ramp-down, the reduction of heating power during the HL transition power should obviously be

significant enough to actually trigger the transition to an L-mode plasma. Note that the rapid reduction of stored thermal energy provides an effective heating term $-\dot{W}_{th} = -dW_{th}/dt > 0$, as the stored thermal energy crosses the separatrix, contributing to $P_{sep} = P_{heat} - \dot{W}_{th} - P_{rad}$, delaying the timing when $P_{sep} < P_{LH}$, with P_{LH} the LH threshold power predicted by the Martin scaling law [45].

In the present simulation, self-consistency of the HL transition is ensured by making sure P_{sep} drops below P_{LH} during the HL transition time window between $t = t_{HL}$ and $t = t_{HL} + \Delta t_{duration\ HL}$. The H factor reference trace is linearly reduced during this time window, leading to a decreasing alpha heating. Furthermore, the Greenwald fraction is changed linearly from $f_{Gw} = 1.2$ to 1 during the HL transition interval. The power conducted over the separatrix P_{sep} comes down to P_{LH} only by the end of the HL transition time window, due to the effective $\dot{W}_{th}$ heating term. In the simulation, reducing the Greenwald fraction during the HL transition is found to increase the margin with respect to a radiative collapse, as calculated self-consistently from the various species densities (assuming the pre-defined impurity concentration traces).

5.1.3. The effect of Z_{eff}. Note that by ramping down the impurity concentrations of He and Xe, to avoid radiative collapse, Z_{eff} decreases throughout the ramp-down (the He concentration is reduced, which is consistent with the reducing number of fusion reactions, reducing the source term for He ions; the W concentration is maintained constant[11]). The resulting Z_{eff} evolution is evaluated self-consistently in RAPTOR. A reduced Z_{eff} leads to a reduced resistivity of the plasma, slowing down current diffusion. This raises an interesting trade-off between the margins with respect to radiative and vertical instabilities: by reducing Z_{eff}, margin with respect to a radiative instability can be improved, at the expense of a slower current diffusion, leading to a more significant increase of ℓ_{i3}, making the plasma more vertically unstable. Tailoring the plasma current density to limit the increase of ℓ_{i3}, by optimization of the time traces of plasma current and elongation, is discussed in section 7.

5.1.4. Heat exhaust constraints. Finally, the reduction of impurity concentrations should not lead to a large increase in the power crossing the separatrix, that needs to be handled by the divertor. Even though this heat load would be transient, a reduced P_{sep} with respect to flat-top values might be required due to the difficulty of maintaining the plasma detached during the ramp-down phase, as reducing density and impurity content complicate efficient dissipation in the SOL. In the present simulation P_{sep} is maintained below 240 MW throughout the H-mode phase (compared to $P_{sep} = 205$ MW during flat-top burning plasma phase). This transient increase in P_{sep} is probably beyond what can be tolerated during ramp-down. Further modeling studies into the simultaneous reduction of alpha power and radiated power, including quantitative heat exhaust constraints, are left for future work.

5.2. Current diffusion dynamics

5.2.1. Peaking of the current density. In figure 5, the current density j_{par}, integrated current density I_{encl} and the loop voltage profile U_{pl} are shown at various times during the ramp-down simulation, first during H-mode and subsequently at two times during the L-mode phase. Close to the initial state of the simulation, the current density profile is relatively broad, with a significant contribution from the bootstrap current driven within the pedestal region. The simulation starts from a stationary state with a fully relaxed current density profile, characterized by a radially flat loop voltage profile. As a consequence, the ohmic current density is self-similar with the neoclassical conductivity profile.

To follow the imposed dI_p/dt, the edge loop voltage is continuously reduced (except for an increase during the HL transition), as illustrated in figure 6.[12] As the edge loop voltage is reduced, to significantly negative values, the overall edge poloidal flux difference is negative. The internal current distribution of the plasma changes with a diffusion time scale that increases with the size of the device and the plasma electron temperature, leading to large values in DEMO with respect to present-day devices. In figure 6, an estimate of the characteristic resistive time is included, by evaluating $\tau_R = \mu_0 (a/2)^2 \langle \sigma_{neo} \rangle$, where a is the minor radius and $\langle \sigma_{neo} \rangle$ is the volume average neoclassical conductivity (including a factor accounting for the impact of trapped particles [46, 47]). Clearly, the time window of the ramp-down ($\sim$ 100s), is small with respect to the resistive time that characterizes the time scale for current diffusion, especially during the H-mode phase ($\tau_R \sim$ 1500s).

As the ramp-down is fast with respect to the current diffusion time scale, the current density evolves into an increasingly non-equilibrated state (U_{pl0}-$U_{pl,edge}$ increases, as evident in figure 6). As the loop voltage becomes peaked, the ohmic current density (which is the dominant plasma current contribution, especially during L-mode), can have a substantially different shape with respect to the neoclassical conductivity profile (and hence $T_e^{3/2}$).

The plot showing the integrated plasma current profiles (I_{encl} in figure 5), shows that the enclosed plasma current at small radii decreases very slowly, due to the slow outward current diffusion. As the plasma volume reduces throughout the ramp-down phase, the central current density rises monotonically throughout the ramp-down (see the time trace

[11] For the ramp-down of the ITER $Q = 10$ baseline scenario, predictive simulations have been performed to assess whether the influx of tungsten into the core can be avoided [7, 12]. Time traces of pellet fuelling and auxiliary heating are expected to have a significant impact on W accumulation. A gradual reduction of pellet fuelling was found to be beneficial to avoid the formation of significant core density gradients and the core influx of W, provided that ELM control is maintained during ramp-down. The present paper does not include predictive simulations for the level and the radial distribution of tungsten.

[12] In figure 6 we can also see a step-like behaviour in the time evolution of the edge loop voltage, which clearly correlates with changes in the ramp-down rate of the plasma volume dV/dt.

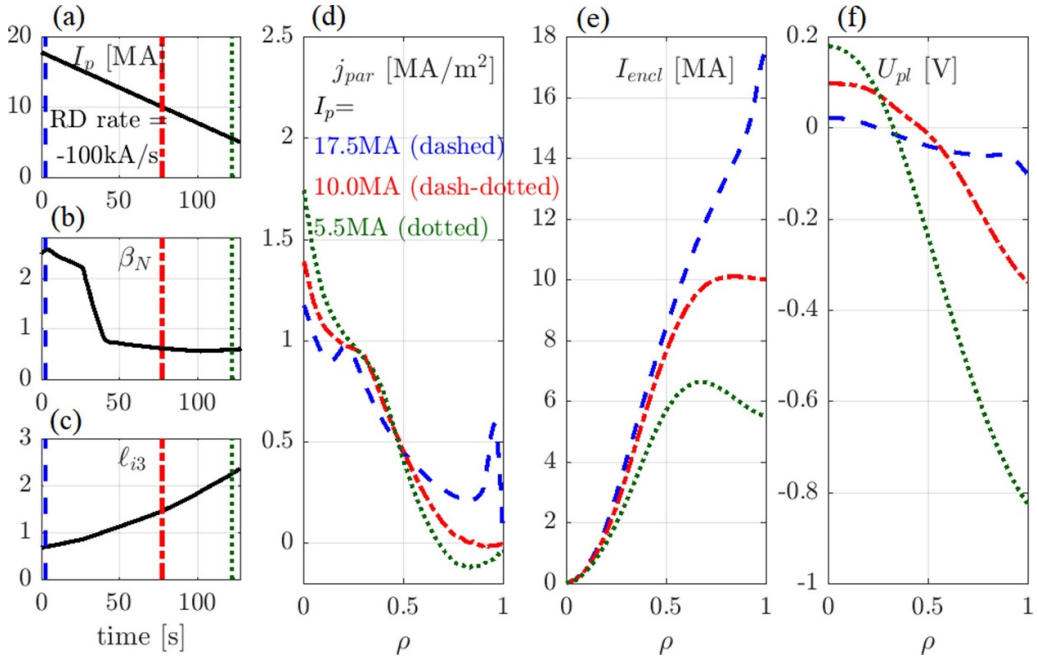

Figure 5. Illustration of current diffusion dynamics during ramp-down, highlighting radial profiles at three different times during the ramp-down. (a) $I_p(t)$ (the three vertical lines correspond to the times for which the radial profiles are shown in (d)–(f)); (b) $\beta_N(t)$; (c) $\ell_{i3}(t)$; (d) parallel current density $j_{par}(\rho)$ at three times during ramp-down, corresponding to $I_p = 17.5$MA, $I_p = 10.0$MA and $I_p = 5.5$MA; (e) idem for the enclosed current $I_{encl}(\rho)$; (f) idem for plasma loop voltage $U_{pl}(\rho)$.

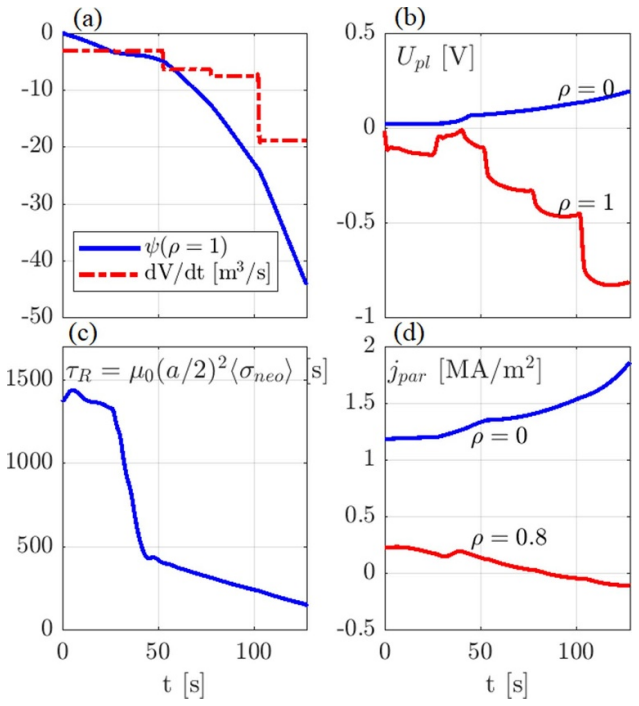

Figure 6. Illustration of current diffusion dynamics during ramp-down. (a) Poloidal flux at the plasma boundary $\psi(\rho = 1, t)$, time derivative of the plasma volume dV/dt; (b) plasma loop voltage $U_{pl}(\rho, t)$ at $\rho = 0$ and $\rho = 1$; (c) resistive time $\tau_R = \mu_0(a/2)^2\langle\sigma\rangle$; (d) parallel current density $j_{par}(\rho, t)$ at $\rho = 0$ and $\rho = 0.8$.

for j_{par} at $\rho = 0$ in figure 6). Nevertheless, the total plasma current evolution (imposed as a Neumann boundary condition for the poloidal flux diffusion equation), needs to be satisfied, leading to a negative current density in the outer plasma (see the time trace for j_{par} at $\rho = 0.8$ in figure 6). The MHD stability of suchlike current density profiles has not been investigated.

As the current density evolves on a slow time scale with respect to the plasma current, the plasma current ramp-down rate dI_p/dt is an effective control parameter to tailor the evolution of the internal inductance ℓ_{i3}, as has been discussed in [11]. In section 7, this feature will be leveraged to maintain the internal inductance below an upper limit given by vertical stability calculations in CREATE-NL.

In [48], a lumped parameter model for the time evolution of the tokamak plasma current and internal inductance has been proposed, with plasma resistance, non-inductive current and boundary voltage or poloidal field coil currents as inputs. The circumstances for a correlation between $d\ell_{i3}/dt$ and dI_p/dt are analytically derived, supporting the use of I_p as a virtual actuator to control the internal inductance.

5.2.2. The impact of sawteeth on current density peaking. The peaking of the current density, as described in the previous section, leads to a continuous decrease of q_0, even though q_{95} is increasing throughout the ramp-down, as shown in figure 4. As a consequence, sawteeth instabilities will likely be triggered at some time during ramp-down. In the present section, we assess the impact of sawteeth on the time evolution of ℓ_{i3}. In figure 7, the early HL, cold L-mode −100 kA/s ramp-down simulation is compared to a simulation where the RAPTOR sawtooth model, first presented in [49], is applied, using the sawtooth models described in [50, 51]. A sawtooth crash is triggered when the magnetic shear at $q = 1$ exceeds a user-defined critical value $s_{q=1,crit}$. In this simulation we set

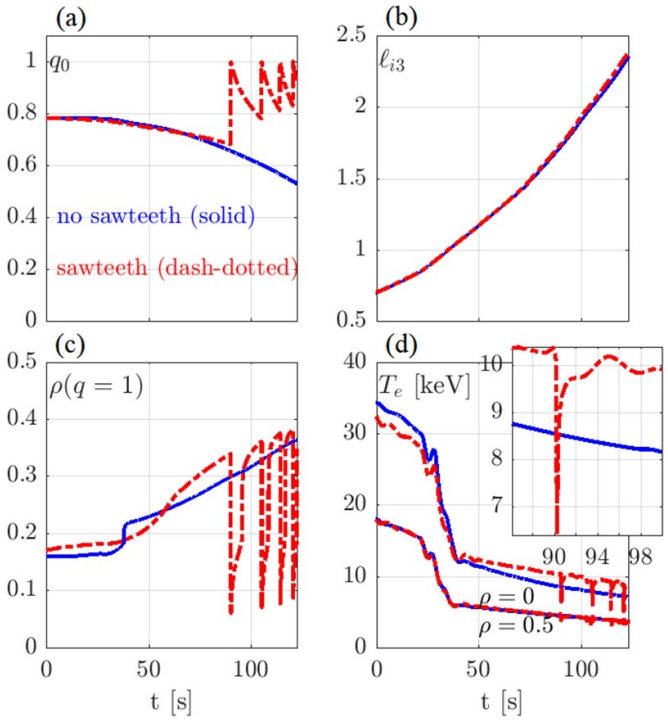

Figure 7. The impact of the sawtooth model on the early HL, cold L-mode, -100 kA s^{-1} ramp-down simulation is illustrated. The simulation without sawteeth is shown in blue solid lines, while the simulation with sawteeth and critical magnetic shear $s_{q=1,crit} = 0.4$ is shown in red dash-dotted lines. For the central temperature, a zoom panel is included to highlight the evolution of T_{e0} after a sawtooth crash. Only a minor impact on the ℓ_{i3} evolution is observed. (a) $q_0(t)$; (b) $\ell_{i3}(t)$; (c) radius of the $q = 1$ surface $\rho_{q=1}(t)$; (d) $T_e(\rho, t)$ at $\rho = 0$ and $\rho = 0.5$.

$s_{q=1,crit} = 0.4$, inspired by the values mentioned for a burning plasma in [52]. The red dash-dotted traces in figure 7 show that the first sawtooth crash is triggered only in the second half of the ramp-down phase, after the plasma transitions to L-mode. The long sawtooth period during the H-mode phase of the plasma is consistent with the fast particle stabilization of sawteeth expected in a burning plasma [50, 53] (resulting in a higher expected value of $s_{q=1,crit}$ compared to present-day devices). The sawtooth module explicitly models the expulsion of energy and particles from inside the $q = 1$ radius after a sawtooth event is triggered. In the the gradient-based transport model settings (described in section 3.3), the central region with high transport has been limited to $\rho_{inv} = 0.2$ for these simulations, assuming that even during the inter-sawtooth interval, core profile flattening can be expected close to the center of the plasma (e.g. like discussed in [31]).

While sawtooth crashes prevent the continuous increase of the central current density, the broadening of the current density profile, through magnetic reconnection occurring on the Alfvén time scale, is localized in the core of the plasma. The impact on the time evolution of the internal inductance is negligible, as illustrated in figure 7. Since the effect of sawtooth is modest under the present modeling assumptions, the sawtooth model is not used in the feasibility and optimization studies discussed further in this paper.

6. Vertical stability for different I_p ramp-rate, HL transition timing and L-mode confinement assumptions

6.1. Modeling results

With the set-up discussed in the previous section, a range of different ramp-down simulations has been performed, with each of the following I_p ramp-down rates: $dI_p/dt = -50$ kA s^{-1}, -100 kA s^{-1}, -150 kA s^{-1}, -200 kA s^{-1}. Note that $dI_p/dt = -200$ kA was used as the starting point of this study, as it is the DEMO reference design value that was also used for the CREATE-NL free boundary equilibrium control simulation in [20]. For each of these ramp-down rates, two simulations are run, differing from one another in terms of HL transition timing and the assumed L-mode confinement quality:

- *Early HL, cold L:* the HL transition is initialized at $t = 0.2t_{final}$. The H factor transitions linearly from $H_{98y,2} = 1$ to $H_{98y,2} = 0.5$, over a duration $\Delta t_{duration\ HL} = 15$ s. These are the same assumptions that have been applied for the simulation in section 5.
- *Late HL, hot L:* the HL transition is initialized at $t = 0.4t_{final}$. The H factor transitions linearly from $H_{98y,2} = 1$ to $H_{98y,2} = 0.75$, over a duration $\Delta t_{duration\ HL} = 15$ s.

By executing the ramp-down simulations for both of these assumptions, a case with a more significant confinement transition earlier in the discharge can be compared with a more gradual confinement transition later in the discharge (giving a rough estimate for the sensitivity to the assumed H factor trace).

The resulting RAPTOR simulations are presented in figure 8. As expected, increasing the absolute value of the I_p ramp-down rate leads to an faster growth of the internal inductance ℓ_{i3}. Furthermore, for each of the ramp-down rates, a delayed HL transition combined with an improved L-mode confinement quality leads to a more significant growth of ℓ_{i3}. Improved confinement during L-mode slows down the diffusion of the central plasma current, causing more significant peaking of the current density.

Let us look in some more detail at the ℓ_{i3} dynamics for the slow ramp-down with $dI_p/dt = -50$ kA s^{-1}, shown in blue in figure 8. Interestingly, we can observe that initially, remaining longer in H-mode leads to slightly reduced values of ℓ_{i3} (blue dotted line) compared to the case with early HL transition (blue solid line). Note however that the increase in growth rate of ℓ_{i3} after the early HL transition is very modest when compared to e.g. the dynamics observed for AUG in Part A [13]. While the late HL transition, hot L-mode case initially maintains lower ℓ_{i3} values, the higher L-mode confinement during the second half of the ramp-down phase eventually leads to a more significant increase of ℓ_{i3} with respect to the early HL transition, cold L-mode case.

Furthermore, increasing the I_p ramp-down rate leads to increasingly negative values of the parallel current density near the edge of the plasma, as shown in figure 9. The -200 kA s^{-1}

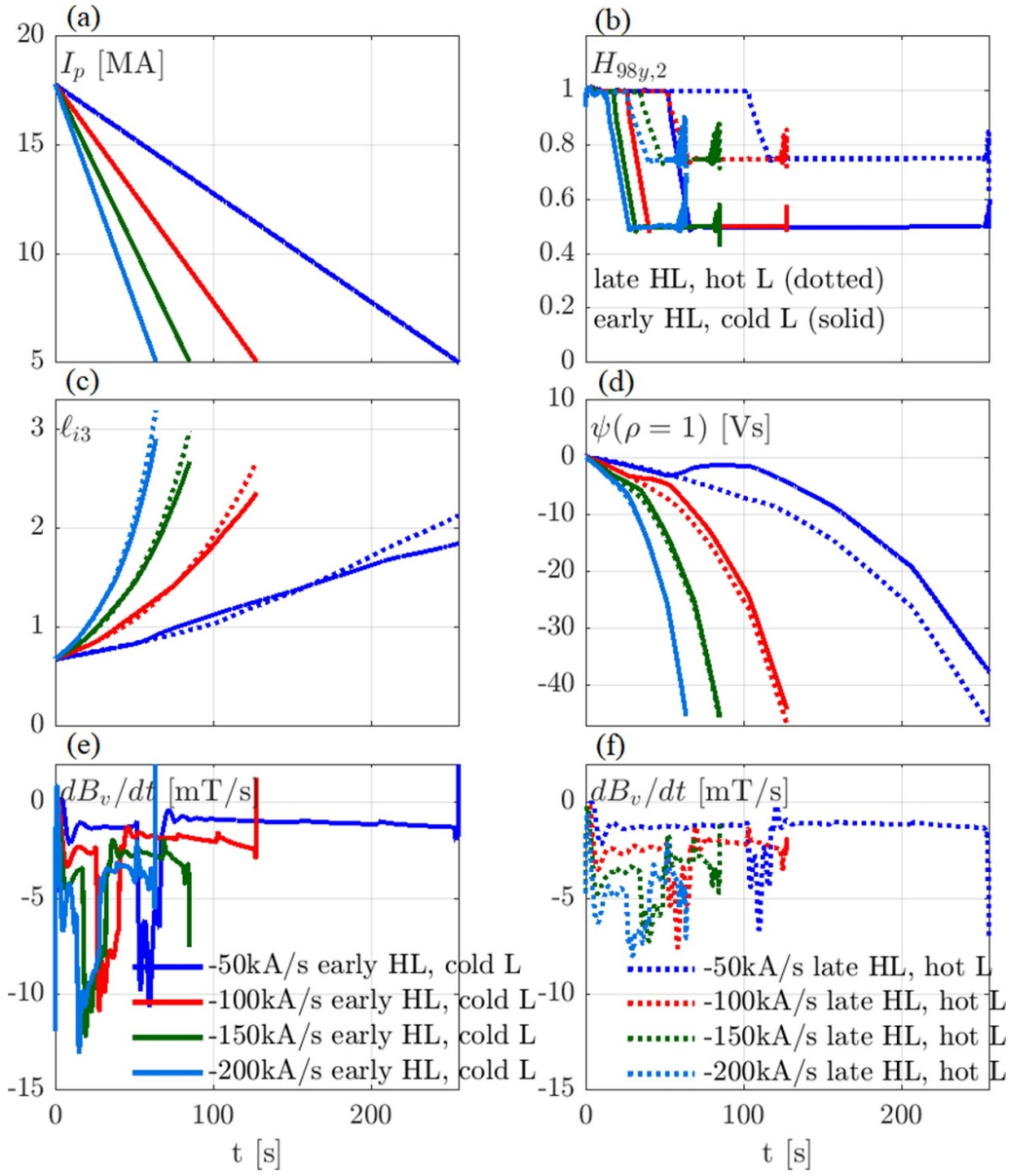

Figure 8. A set of RAPTOR simulations for different ramp-down rates $dI_p/dt = -50\,\mathrm{kA\,s^{-1}}$ (blue), $-100\,\mathrm{kA\,s^{-1}}$ (red), $-150\,\mathrm{kA\,s^{-1}}$ (green), $-200\,\mathrm{kA\,s^{-1}}$ (light blue). For each ramp-down rate, two assumptions for the $H_{98y,2}$ time evolution are considered (early HL transition, cold L-mode in solid lines: $t_{HL} = 0.2t_{final}$, $H_{98y,2} = 0.5$ during L-mode; late HL transition, hot L-mode in dotted lines: $t_{HL} = 0.4t_{final}$, $H_{98y,2} = 0.75$ during L-mode). (a) $I_p(t)$; (b) $H_{98y,2}(t)$; (c) $\ell_{i3}(t)$; (d) $\psi(\rho=1,t) - \psi(\rho=1,t=0\,\mathrm{s})$ at $\rho=1$; (e), (f) time derivative of the vertical magnetic field $dB_v(t)/dt$.

ramp-down with late HL transition features the largest ratio between average resistive diffusion time τ_R and the ramp-down time t_{final}, and the most negative values of j_{par}. Looking at the profile of the enclosed plasma current at the final time step of the simulation (when $I_p = 5\,\mathrm{MA}$), we observe a significant negative current with a magnitude of about 3 MA in the outer plasma region $\rho > 0.7$. As negative edge loop voltages are applied for all modeled ramp-downs (except for a small time interval in the $-50\,\mathrm{kA\,s^{-1}}$ ramp-down with early HL transition), the expected edge poloidal flux difference is negative for all cases. Interestingly, these simulations do not indicate a significant difference of the edge poloidal flux swing that is required for the different I_p ramp-down rates, as quantified in panel (d) of figure 8. Note that the edge poloidal flux difference is not equal to the flux swing of the central solenoid, as the flux due to the plasma external inductance and the flux due to changing currents in the poloidal field coils need to be accounted for (especially when changing the plasma shape). However, these simulations indicate that significant recharging of the central solenoid can be expected during ramp-down for DEMO.

To ensure radial position control, the time derivative of the vertical magnetic field must stay below an upper limit, depending on coil voltage limits imposed by power supplies and/or the superconductor. While we have presently no upper limit value available, we evaluate dB_v/dt with equation (1) for the

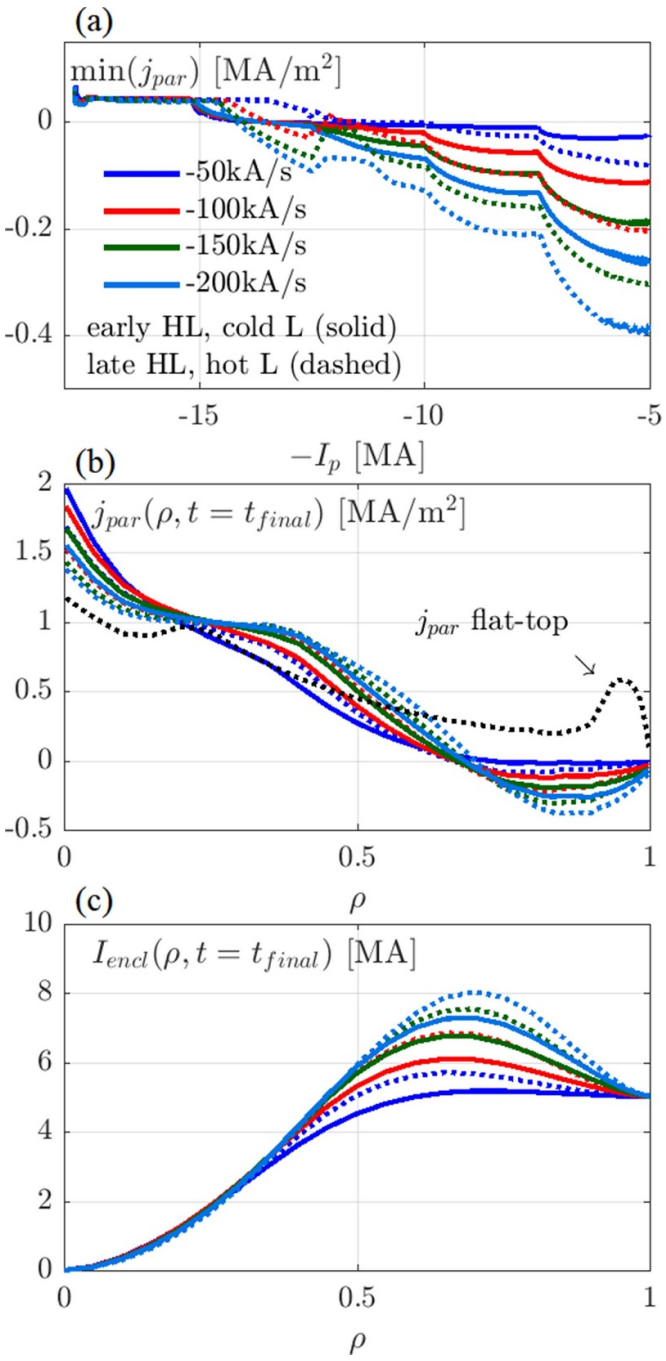

Figure 9. A set of RAPTOR simulations for different ramp-down rates $dI_p/dt = -50\,\mathrm{kA\,s^{-1}}$ (blue), $-100\,\mathrm{kA\,s^{-1}}$ (red), $-150\,\mathrm{kA\,s^{-1}}$ (green), $-200\,\mathrm{kA\,s^{-1}}$ (light blue). For each ramp-down rate, two assumptions for the $H_{98y,2}$ time evolution are considered (early HL, cold L-mode in solid lines: $t_{HL} = 0.2t_{final}$, $H_{98y,2} = 0.5$ during L-mode; late HL, hot L-mode in dotted lines: $t_{HL} = 0.4t_{final}$, $H_{98y,2} = 0.75$ during L-mode). (a) $\min_\rho(j_{par}(\rho,t))$; (b) $j_{par}(\rho)$ at $t = 0\,\mathrm{s}$ and $t = t_{final}$; (c) enclosed plasma current $I_{encl}(\rho)$ at $t = t_{final}$.

different simulations, as shown in figure 8. The time derivative dB_v/dt reaches the largest absolute values during the HL transition (as expected from the β_p dependence in equation (1)). Interestingly, the best-case scenario $H_{98y,2}$ trace regarding vertical stability (early HL, cold L) is the most demanding regarding radial position control, with the most significant peak in the dB_v/dt trace. To disentangle the effects of HL timing and L-mode confinement on the dB_v/dt trace, we also executed a simulation with late HL transition to cold L-mode (for the $-100\,\mathrm{kA\,s^{-1}}$ case). For this additional simulation, dB_v/dt values similar to the early HL transition to cold L-mode case have been obtained, indicating a modest impact on radial position control of the HL timing itself (under the assumption that the Greenwald fraction during H-mode can be maintained constant).

Table 2. From free boundary equilibrium control calculations with CREATE-NL [19], the above combinations of (I_p, κ, ℓ_{i3}) are considered controllable, as reported in [20]. For a given plasma current, the elongation and internal inductance values provide an upper constraint on the stable operating envelope.

I_p [MA]	ℓ_{i3}	β_{pol}	κ
19.6	<0.90	1.10	<1.68
17.5	<1.00	1.10	<1.56
15.0	<1.10	1.05	<1.50
12.5	<1.25	1.00	<1.45
10.0	<1.40	1.00	<1.40
7.5	<1.60	0.10	<1.40
5.0	<1.70	0.10	<1.35

6.2. Comparison of RAPTOR-predicted ℓ_{i3} versus CREATE-NL vertical stability limit

6.2.1. CREATE-NL vertical stability limit. In [20], free boundary equilibrium control calculations with CREATE-NL [19] are presented for the diverted phase of the DEMO plasma ramp-up and ramp-down. For the ramp-down, the limits to a vertically stable operating envelope are mapped out with respect to the plasma current I_p, elongation κ and internal inductance ℓ_{i3}. The resulting sequence of triplets (I_p, κ, ℓ_{i3}) of controllable operating parameters is repeated in table 2. Each of these three parameters play an important role in the assessment of vertical stability: while a degraded vertical control efficiency can be anticipated for an increased internal inductance ℓ_{i3}, corresponding to a more significant peaking of the current density, this tendency can be counteracted by adjusting the plasma shape, reducing the elongation. Furthermore, controllability of the vertical position improves at lower plasma current, as the coil currents for vertical stability control in the CREATE-NL model for DEMO are more effective to counteract vertical position excursions at lower plasma current [20].

Considering the upper limits for internal inductance ℓ_{i3} and elongation κ for a given plasma current I_p (as summarized in table 2), the potential of different ramp-down rates to maintain the internal inductance below the upper limit for vertical controllability can now be assessed. For the purpose of the feasibility study presented here and the optimization introduced in the next section, we employ these values to extract a constraint on the internal inductance, dependent on the plasma current value. We assume that the plasma can be maintained vertically stable if $\ell_{i3} < f_{\mathrm{margin}}\ell_{i3\ \mathrm{CREATE}}(I_p)$. We include a margin factor $f_{\mathrm{margin}} > 1$, as the present constraint $\ell_{i3\ \mathrm{CREATE}}(I_p)$ is a

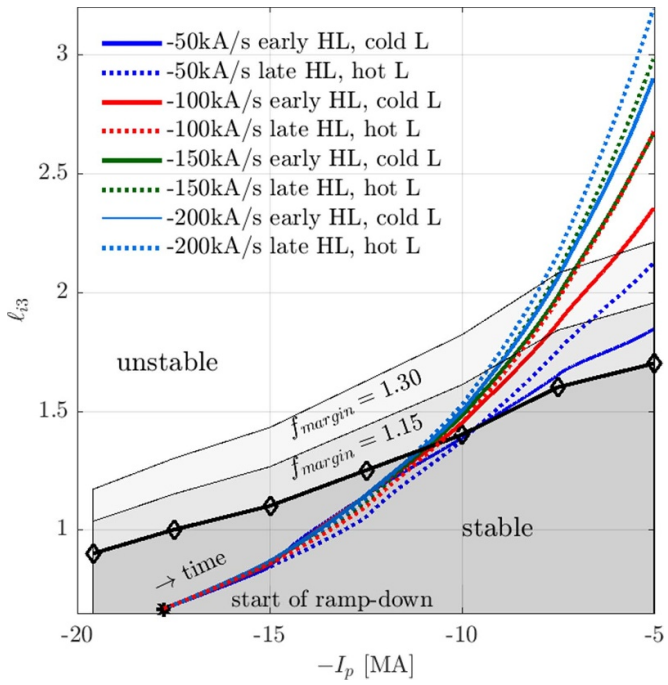

Figure 10. Time traces of ℓ_{i3} within the $(-I_p, \ell_{i3})$ plane, for the RAPTOR simulations shown in figure 8. The stability limit $f_{\text{margin}}\ell_{i3\ \text{CREATE}}(I_p)$ allows to assess the margin with respect to the vertical stability limit obtained in CREATE-NL.

conservative assessment, not an optimized limit. Various considerations could increase the maximum allowed ℓ_{i3}.

- Optimizing position and shape control, while using the consistent kinetic profile evolution, is expected to provide some improvement with respect to vertical controllability.
- Inclusion of in-vessel coils in the DEMO design would facilitate more effective vertical control.
- A faster decrease of elongation κ with respect to the reference in [20] improves vertical controllability for a given plasma current.

The vertical stability constraint $\ell_{i3\ \text{CREATE}}(I_p)$ is indicated in figure 10, with the diamond symbols representing the equilibria from CREATE-NL that are introduced in table 2. Allowing for some margin with respect to this conservative CREATE-NL result, the lines with margin factor $f_{\text{margin}} = 1.15$ and 1.30 are also shown. The dark grey region with $\ell_{i3} < \ell_{i3\ \text{CREATE}}(I_p)$ is the region where vertical stability can be guaranteed, while the white region $\ell_{i3} > 1.30\ell_{i3\ \text{CREATE}}(I_p)$ contains operating points that can likely not be maintained vertically stable. Note that the x-axis is $-I_p$, so that moving to the right on the abscissa corresponds to progressing time during the ramp-down phase. Later in the ramp-down, at lower plasma currents, a larger internal inductance can be maintained vertically stable.

6.2.2. Comparison to modeled ℓ_{i3} traces. Let us now superimpose the ℓ_{i3} traces modeled in RAPTOR on the $(-I_p,\ell_{i3})$ plot in figure 10. For each of the considered ramp-down rates $dI_p/dt = -50\,\text{kA}\,\text{s}^{-1}$, $-100\,\text{kA}\,\text{s}^{-1}$, $-150\,\text{kA}\,\text{s}^{-1}$, $-200\,\text{kA}\,\text{s}^{-1}$, the two assumptions for the $H_{98y,2}$ time evolution introduced in section 6 are considered: early HL transition to cold L-mode versus late HL transition to hot L-mode. The maximum values of ℓ_{i3} reached at the final time of the simulation (for $I_p = 5\,\text{MA}$) are shown in table 3. As a first conclusion, we can observe that the tendency of the plasma to peak the current density during the ramp-down phase leads to a more significant increase of ℓ_{i3} compared to the increase of the constraining value $\ell_{i3\ \text{CREATE}}$, even for a conservative ramp-rate of $dI_p/dt = -50\,\text{kA}\,\text{s}^{-1}$. However, allowing for some margin on the vertical stability constraint (justified by the reasons listed earlier), the $dI_p/dt = -50\,\text{kA}\,\text{s}^{-1}$ ramp-down simulations stay below upper limits with f_{margin} respectively 1.15 and 1.30. For the fastest ramp-down assumption ($dI_p/dt = -200\,\text{kA}\,\text{s}^{-1}$), both H factor trace assumptions lead to a severe violation of the upper ℓ_{i3} limit with $f_{\text{margin}} = 1.30$. Also for the simulations with intermediate I_p ramp-down rates ($dI_p/dt = -150\,\text{kA}\,\text{s}^{-1}, -100\,\text{kA}\,\text{s}^{-1}$), the upper ℓ_{i3} limit with $f_{\text{margin}} = 1.30$ is violated. In the following section, we will attempt to optimize the plasma current trace and the plasma shaping evolution to bring the ℓ_{i3} trace below the upper constraint, with f_{margin} either 1.15 and 1.30.

Table 3. Final (maximum) value of the internal inductance ℓ_{i3} for the RAPTOR simulations shown in figure 8.

dI_p/dt (kA s^{-1})	t_{final} (s)	$\ell_{i3\ \text{final}}$ (early HL, cold L)	$\ell_{i3\ \text{final}}$ (late HL, hot L)
−50	256	1.84	2.12
−100	128	2.35	2.68
−150	85	2.67	2.98
−200	64	2.90	3.19

7. Optimized I_p and shaping evolution to avoid vertical instability

In the present section, feasible DEMO ramp-down scenarios are searched for by numerical solution of an optimal control problem for the ramp-down phase. The mathematical formulation and solution procedure is discussed in section 7.1, while the actual results are presented in section 7.2.

7.1. Formulation of the optimization problem

7.1.1. Cost function. Loosely speaking, the aim is to ramp down the plasma current I_p as quickly as possible, while satisfying all physical and technical constraints. Since the plasma density should decrease proportional to I_p to avoid density limit excursions and since the fusion power is proportional to the square of the plasma density, a fast decrease of I_p corresponds to a fast decrease of the plasma thermal energy (also the confinement time is expected to decrease proportional to I_p). A fast I_p decrease hence reduces the potential impact of depositing the stored thermal energy on the reactor vessel first

wall. Furthermore, the electromagnetic forces acting on the vessel after plasma disruption are proportional to I_p^2. To reflect these considerations, the time integral of the plasma current is chosen as a cost function:

$$J_{I_p} = \nu_{I_p} \int_0^{t_{\text{final}}} I_p(t)\, dt. \tag{4}$$

The objective of the optimization problem is to minimize J_{I_p}. The factor ν_{I_p} is chosen to have a cost function around unity for the initial condition for the ramp-down traces.

7.1.2. Constraint functions. An extensive set of physical and technical limits constrain the ramp-down phase:

- *Density limit:* as the time evolution of the plasma current $I_p(t)$ is adjusted during the optimization, the reference density trace $n_{el,\ ref}(t)$ (defined in section 3.3) is updated after each iteration step, to keep the allowed Greenwald fraction time trace unchanged throughout the optimization procedure. The present work does not assess whether sufficient pumping capacity is available to reduce the density at the required rates.
- *Vertical stability limit:* $\ell_{i3} < f_{\text{margin}} \ell_{i3,\ \text{CREATE}}(I_p)$, as discussed before. Note that by optimizing the plasma current, both the internal inductance ℓ_{i3} and the upper limit $\ell_{i3,\ CREATE}(I_p)$ can be adjusted. The corresponding constraint in the optimization problem is formulated as $c_1 = \ell_{i3} - f_{\text{margin}} \ell_{i3\ \text{CREATE}}(I_p) < 0$ and should be enforced over the entire ramp down interval.
- *Ideal MHD stability:* to maintain a margin with respect to ideal MHD limits, a constraint is added to enforce a monotonic increase of q_{95} while $q_{95} < 4.5$ (assuming that when $q_{95} > 4.5$, a decrease can be safely allowed). This constraint is included as plasmas with a lower q_{95} value are more prone to MHD instabilities, since they operate closer to the ideal MHD limit. Note that this is not a hard limit and could be relaxed. The corresponding constraint in the optimization problem is formulated as $c_2 = -\dot{q}_{95} < 0$ and should be active only for those time points when $q_{95} < 4.5$.

Through the formalism introduced in [54], the state constraints $c_1(x(t)) < 0$ and $c_2(x(t)) < 0$ (dependent on the plasma state $x(t)$, which contains the radial distribution of T_e, n_e and ψ, as evolved by RAPTOR) are formulated as integral constraints (instead of a separate constraint for each t_k):

$$\mathscr{C}_i = \left(\int_{t_0}^{t_f} \left(\max\left\{0, w_i c_i(x(t))\right\}\right)^2 dt - \varepsilon \right) \leqslant 0. \tag{5}$$

The weight w_i is set to unity for those times where the corresponding constraint is active (for those times when $q_{95} < 4.5$ for c_2). We obtain the two integral constraints: $\mathscr{C}_{\ell_{i3} < f_{\text{margin}} \ell_{i3\ \text{CREATE}}(I_p)} \leqslant 0$ and $\mathscr{C}_{\dot{q}_{95} > 0} \leqslant 0$.

7.1.3. Optimization variables. The actuator traces that are optimized to minimize the cost function, while satisfying the constraints, are the plasma current $I_p(t)$ and the elongation of the plasma $\kappa(t)$. Within the optimization problem formulation, the actuator traces $u_i(t)$ ($u_1(t) = I_p(t)$ and $u_2(t) = \kappa(t)$) are parametrized by the vector $[p_{1,1}\ \ldots\ p_{1,n_1}\ p_{2,1}\ \ldots\ p_{2,n_2}]^T$. By multiplication with a set of piecewise linear basis functions (respectively n_1 functions $P_{1j}(t)$ and n_2 functions $P_{2j}(t)$), followed by summation, the actuator traces $u_i(t)$ are recovered:

$$u_i(t) = \sum_j^{n_i} P_{ij}(t)\, p_{i,j}. \tag{6}$$

The initial and final values of I_p and κ are maintained unchanged by fixing the parameters $p_{1,1}$, p_{1,n_1}, $p_{2,1}$ and p_{2,n_2}. The remaining parameters are assembled in the optimization vector $\mathbf{p} = [p_{1,2}\ \ldots\ p_{1,n_1-1}\ p_{2,2}\ \ldots\ p_{2,n_2-1}]^T$. The optimization variables in this vector $\mathbf{p}$ contain the values of the actuator time traces on a set of knot points (the points indicated with star symbols in figure 11, excluding the initial and final time points) and are varied in each iteration of the optimization routine.

The timing of the HL transition is maintained fixed throughout the optimization. The simulations in section 6 and AUG experiments in Part A [13], as well as cross-machine analysis in [11], highlight the importance of this parameter in determining the ramp-down dynamics. In the present work, sensitivity to this parameter has been tested by running optimizations for different assumptions regarding the HL timing. A natural follow-up of the present work would be the inclusion of the HL timing as an optimization variable, as demonstrated in section 4.4 of [55]. Auxiliary current drive, e.g. ECCD, has not been considered as an actuator to optimize the current density profile in the present work. Note that EC deposition control could also be needed to avoid tungsten accumulation in the core, or for NTM control [10].

7.1.4. Using the elongation trace κ as an optimization variable. As the equilibrium impacts the radial transport equations through geometric coefficients in the diffusion PDEs, the time evolution of the elongation κ can be used as an optimization variable, to impact the plasma state dynamics. In RAPTOR, these metrics, stacked together in the vector $\mathbf{g}$, are calculated from the output files of a CHEASE equilibrium solution. From the CREATE-NL equilibrium solutions introduced in section 3.5, a sequence of metrics $\mathbf{g}_\kappa$ for seven different values of plasma elongation κ is obtained. During a ramp-down with constant ramp rate dI_p/dt, $\mathbf{g}$ for intermediate time points is evaluated through linear interpolation in time.

We attempt to optimize the time evolution of the plasma shape, by finding the optimum time trace of the elongation $\kappa(t)$. The fact that the dependencies of the geometric factors $\mathbf{g}$ on κ are not analytically available, has consequences for the optimization routine:

- Cost and constraint function gradients $\frac{\partial J}{\partial \mathbf{p}}$ and $\frac{\partial \mathscr{C}}{\partial \mathbf{p}}$ have to be evaluated numerically with finite differencing and cannot be evaluated analytically, slowing down the optimization.

- Lacking a coupled Grad-Shafranov solver, a consistent evaluation of the updated metrics **g** for a changed κ cannot be obtained within the optimization routine.

After each iteration step, the geometric factors **g** have to be recalculated to match the new trial of the time evolution of the elongation κ. A linear interpolation scheme is applied to update the metrics **g**. The two reference equilibria with most similar elongation κ are identified (out of the set of CREATE-NL equilibria $\kappa_{ref,i}$): $\kappa_{ref\ 1} < \kappa_{opt} < \kappa_{ref\ 2}$. Then, a linear interpolation in κ is applied to obtain the metric vector **g**:

$$\mathbf{g}_{\kappa_{opt}} = \mathbf{g}_{\kappa_{ref\ 1}} + \frac{\kappa_{opt} - \kappa_{ref\ 1}}{\kappa_{ref\ 2} - \kappa_{ref\ 1}} \left(\mathbf{g}_{\kappa_{ref\ 2}} - \mathbf{g}_{\kappa_{ref\ 1}}\right). \tag{7}$$

Once an optimized ramp-down scenario is found, the adequacy of this linear interpolation scheme can be checked by running a set of CHEASE simulations for time points along the optimized trajectory, as illustrated in section 7.4.

7.1.5. Ramp-down optimal control problem. To summarize, the ramp-down optimal control problem can be written as:

$$\min_{\mathbf{p}} J_{I_p}(u_i(t)) \quad \forall t \in [t_0, t_{final}] \text{ (cost)} \tag{8a}$$

$$\text{subject to } f(\dot{x}(t), x(t), u(t)) = 0 \quad \forall t \in [t_0, t_{final}] \text{ (state)} \tag{8b}$$

$$u_i(t) = \sum_j^{n_i} P_{ij}(t)\, p_{i,j} \text{ (actuator parametrization)} \tag{8c}$$

$$A_{ineq}\mathbf{p} \leqslant b_{ineq} \text{ (actuator limits)} \tag{8d}$$

$$\mathscr{C}_{\ell_{i3} < f_{\text{margin}}\ell_{i3\ \text{CREATE}}(I_p)} \leqslant 0 \text{ and } \mathscr{C}_{\dot{q}_{95}>0} \leqslant 0 \text{ (state constraints).} \tag{8e}$$

The RAPTOR state evolution equation f defines the time evolution of the plasma state $x(t)$. The actuator limits equation (8*d*) are included to impose both $I_p(t)$ and $\kappa(t)$ to be monotonically decreasing. Note that this condition can be written as a linear inequality constraint on **p**, as $du_i/dt \leqslant 0$ translates directly to $\sum_j^{n_i} dP_{ij}(t)/dt p_{i,j} \leqslant 0$. At this stage, no minimum time derivative is set. Position and shape control studies including the poloidal field coil currents are required to establish how fast plasma current and plasma shaping can be changed during the ramp-down phase.

The algorithm applied to solve the non-linear, constrained optimization problem formulated in equations (8*a*)–(8*e*) is sequential quadratic programming (SQP) [56], as implemented in the Matlab function `fmincon`. This algorithm was applied before in [1, 54]. Even though cost and constraint function gradient information has to be obtained numerically, the fast run time of a single RAPTOR simulation allows to maintain the full solution of the non-linear optimization problem computationally tractable (a few hours on a single CPU).

Generally speaking there is no guarantee that the obtained optimum trajectory is a global optimum. Rerunning the optimization from different initial conditions allows to increase confidence in the obtained optimum solution. Finally, the selection of the number of optimization variables needs to give the optimizer enough degrees of freedom to be able to find an optimum, while a too high dimensionality leads to the risk of over-fitting with respect to specific settings of model parameters. Verifying the obtained optimum trajectory with more complete integrated modeling tools could increase confidence in the obtained optimum.

7.2. Optimized DEMO ramp-down scenarios

A set of optimized DEMO ramp-down scenarios is summarized in figure 11, with different assumptions regarding the total ramp-down time window and the time evolution of the reference $H_{98y,2}$:

(i) $dI_p/dt = -100\,\text{kA}\,\text{s}^{-1}$; late HL transition, hot L-mode;
(ii) $dI_p/dt = -150\,\text{kA}\,\text{s}^{-1}$; early HL transition, cold L-mode;
(iii) $dI_p/dt = -200\,\text{kA}\,\text{s}^{-1}$; early HL transition, cold L-mode.

The respective trajectories given as initial conditions to the optimizer are the corresponding RAPTOR simulations shown in figures 8 and 10. The red dash-dotted traces in figure 11 represent the optimum found for the optimization problem formulated in equations (8*a*)–(8*e*), with $\mathscr{C}_{\ell_{i3} < f_{\text{margin}}\ell_{i3\ \text{CREATE}}(I_p)} \leqslant 0$ and $\mathscr{C}_{\dot{q}_{95}>0} \leqslant 0$ as active constraints. The second constraint is added as a significant reduction of the elongation during the early ramp-down can lead to low q_{95} values that could compromise ideal MHD stability. To counteract this effect, $dq_{95}/dt > 0$ when $q_{95} < 4.5$ is imposed, ensuring q_{95} increases monotonically during the early ramp-down.

For cases (1) and (2), a feasible solution is found with $f_{\text{margin}} = 1.15$, while for case (3), f_{margin} has to be raised to 1.30 to find a feasible solution. Both I_p and κ are approximated by linear segments, parametrized by three intermediate knot points (at the intersection of linear segments). The end points are maintained equal to the initial condition, while the values of the knot points constitute the optimization variables (6 optimization variables in total).

For each of the three cases, the optimized $I_p(t)$ and $\kappa(t)$ trajectories feature both a sharp initial decrease in the first segment of the ramp-down. The initial fast reduction of I_p leads to a very fast increase of ℓ_{i3}. However, the fast decrease of I_p also leads to a fast increase of the upper limit $f_{\text{margin}}\ell_{i3\ \text{CREATE}}(I_p)$. Furthermore, the decrease of the I_p and κ ramp-rates at the first knot point leads to a knee point in the $\ell_{i3}(t)$ trace. For the three cases, an optimum trajectory is found that avoids a violation of the vertical stability constraint throughout the entire ramp-down phase, while featuring a monotonic increase of q_{95} for $q_{95} < 4.5$.

To illustrate the importance of the $\mathscr{C}_{\dot{q}_{95}>0} \leqslant 0$ constraint, the green dashed traces in figure 11 represent the ramp-down traces that are obtained if the optimum I_p trace is applied,

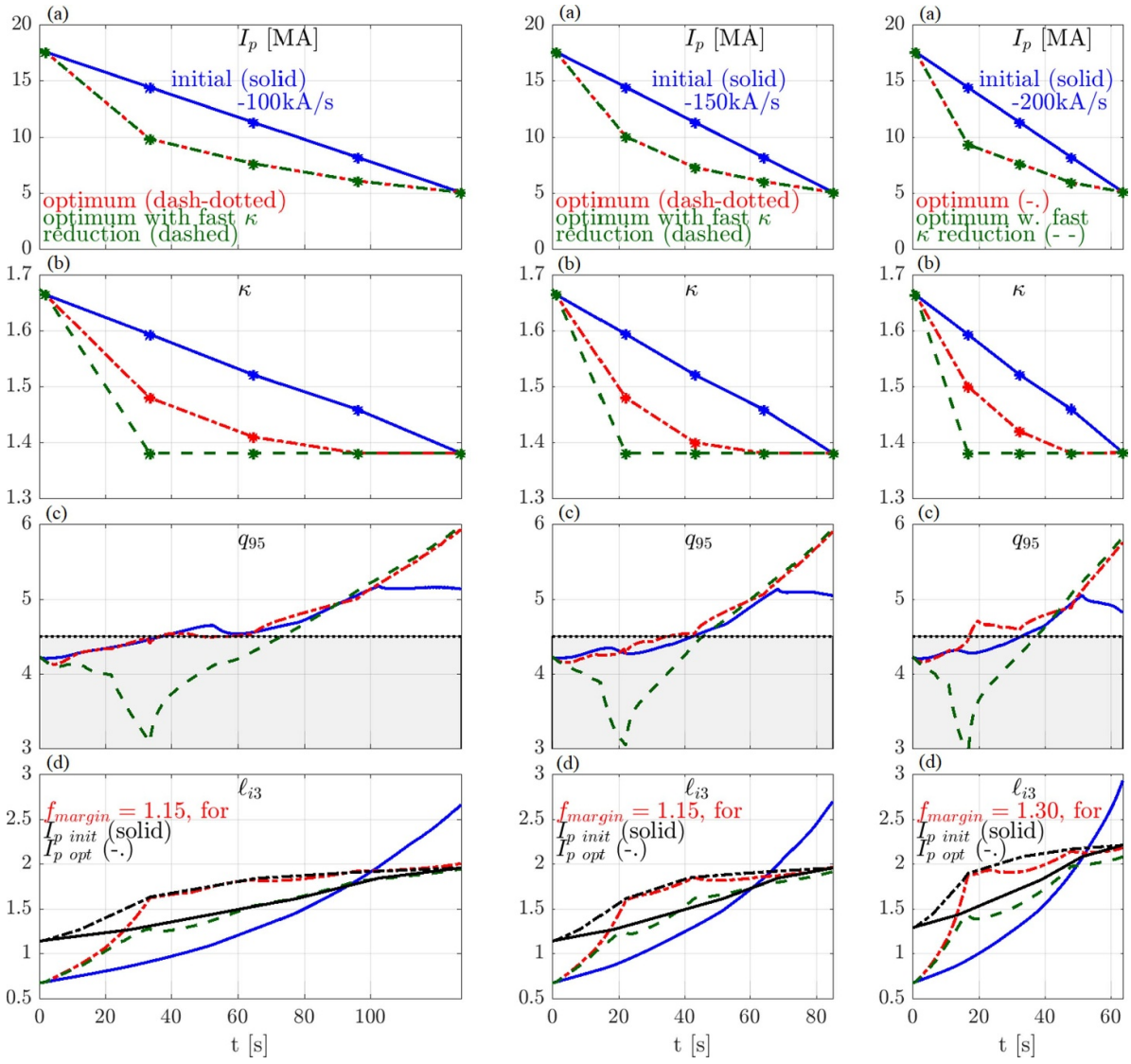

Figure 11. Initial and optimized time traces for three DEMO ramp-downs: (1) $dI_p/dt = -100\,\mathrm{kA\,s^{-1}}$; late HL transition, hot L-mode; (2) $dI_p/dt = -100\,\mathrm{kA\,s^{-1}}$; early HL transition, cold L-mode; (3) $dI_p/dt = -200\,\mathrm{kA\,s^{-1}}$; early HL transition, cold L-mode. The time traces of the initial ramp-down simulation are shown in solid blue lines. The time traces of the ramp-down simulation with optimized I_p and κ trajectories are shown in red dash-dotted lines. The green dashed lines correspond to a ramp-down simulation with an I_p trace corresponding to the optimum, and a fast reduction of the elongation κ, leading to a violation of the constraint on q_{95}. Feasible ramp-down traces are found with $f_{\mathrm{margin}} = 1.15$ for (1) and (2) and with $f_{\mathrm{margin}} = 1.30$ for (3). (a) $I_p(t)$; (b) elongation $\kappa(t)$; (c) $q_{95}(t)$ (the grey area indicates $q_{95} < 4.5$, where a constraint penalizes a negative time derivative dq_{95}/dt); (d) $\ell_{i3}(t)$; the vertical stability constraint from CREATE-NL is shown in black lines, the applied f_{margin} factor is indicated in red text (note that two constraint curves are shown corresponding to the two different I_p traces, respectively the solid line of the initial trajectory and the dash-dotted line of the optimized trajectory).

while reducing κ immediately to the minimum value during the first time segment. A fast reduction of the elongation is beneficial to increase the vertical controllability of the plasma. Additionally, we observe that the fast κ reduction leads to a significant reduction of the internal inductance, providing a larger margin with respect to the upper limit $f_{\mathrm{margin}}\ell_{i3\ \mathrm{CREATE}}(I_p)$. However, the fast reduction of elongation leads to a significant decrease of q_{95}, potentially compromising MHD stability (as observed in the ASDEX Upgrade experiment described in [13]).

We conclude that the non-linear optimization routine manages to find a feasible ramp-down trace, optimizing the I_p and κ traces to satisfy both constraints $\mathscr{C}_{\ell_{i3} < f_{\mathrm{margin}}\ell_{i3\ \mathrm{CREATE}}(I_p)} \leqslant 0$ and $\mathscr{C}_{q_{95}>0} \leqslant 0$. In the next section, we investigate in more detail the impact of respectively I_p and κ on the time evolution of the internal inductance.

7.3. Interpretation of the impact of the optimum I_p and κ traces on ℓ_{i3}

To understand better the dynamics underlying the obtained optimum trajectory, we study in more detail the optimized I_p and κ traces for the case with $dI_p/dt = -100\,\mathrm{kA\,s^{-1}}$, late HL transition, hot L-mode in figure 11. Various simulations

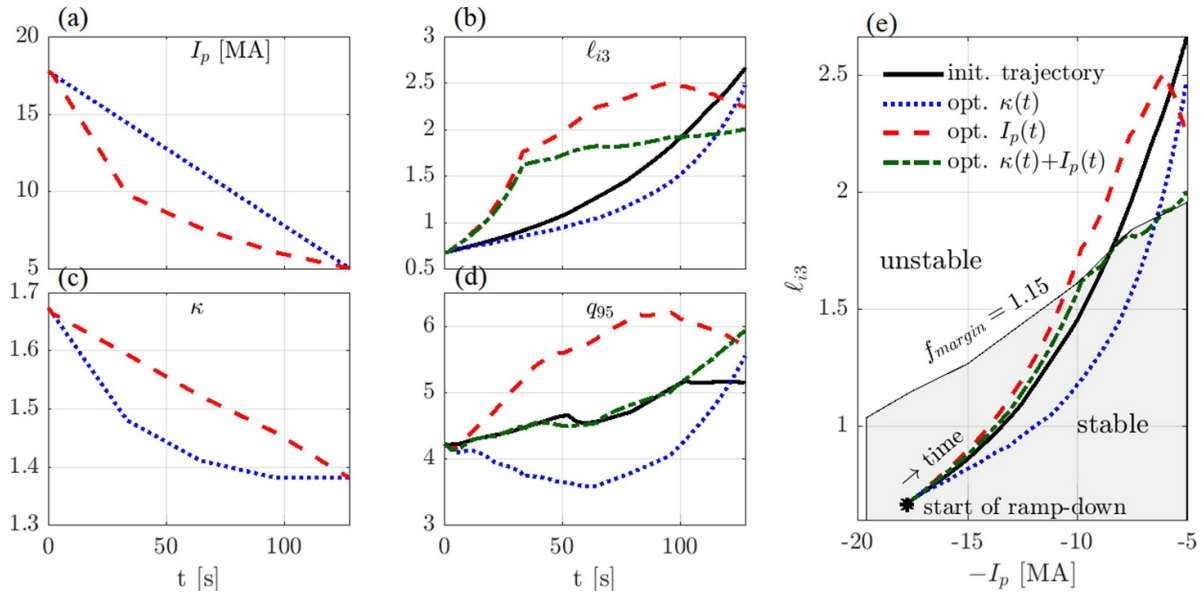

Figure 12. A set of ramp-down simulations is presented to improve our understanding of the dynamics underlying the obtained optimum trajectory (for the case with $dI_p/dt = -100\,\mathrm{kA\,s^{-1}}$, late HL transition, hot L-mode in figure 11). The initial, non-optimized ramp-down is shown in black solid lines. The case with optimized I_p and κ evolution is presented in green dash-dotted lines. A simulation applying the initial I_p evolution and the optimized κ evolution and a simulation with the optimized I_p evolution and the initial κ evolution are shown in blue dotted lines and red dashed lines respectively. (a) $I_p(t)$; (b) $\ell_{i3}(t)$; (c) elongation $\kappa(t)$; (d) $q_{95}(t)$; (e) ℓ_{i3} versus $-I_p$.

are performed to understand both the individual and the joint impact of the optimized I_p and κ traces, as presented in figure 12 and explained below.

- **Initial ramp-down trajectory with constant dI_p/dt and $d\kappa/dt$** (black solid trace)
- **Optimized shaping evolution $\kappa(t)$, while maintaining the initial $I_p(t)$ evolution with constant dI_p/dt** (blue dotted trace)
  The faster reduction of elongation κ leads to a reduction of ℓ_{i3} compared to the initial ℓ_{i3} trace, throughout the entire simulation time window. Note however that the value of q_{95} reduces below its flat-top value, potentially compromising ideal MHD stability.
- **Optimized plasma current evolution $I_p(t)$, while maintaining the initial $\kappa(t)$ evolution with constant $d\kappa/dt$** (red dashed trace)
  When maintaining the plasma shaping evolution unchanged, the fast plasma current reduction leads to larger values of of the internal inductance $\ell_{i3}(t)$ throughout most of the simulated time window, even though the final value of ℓ_{i3} is reduced. The reduction of the I_p ramp-rate around $I_p = 10\,\mathrm{MA}$ leads to a knee point in the internal inductance ℓ_{i3} trace. This illustrates that I_p is an effective actuator to tailor the time evolution of ℓ_{i3}. For the same shaping trajectory, the lower plasma currents lead to a more significant increase of q_{95}.
- **Optimized plasma current $I_p(t)$ and shaping evolution $\kappa(t)$** (green dash-dotted trace)
  Application of the individual optimized traces of I_p and κ is insufficient to maintain $\ell_{i3} < 1.15\ell_{i3\ \mathrm{CREATE}}(I_p)$. However, as shown in the right panel of figure 12, the combined impact of both actuators is successful in satisfying the constraint, while q_{95} is monotonically increasing, remaining above the flat-top value.

7.4. Consistency of the optimized evolution of shaping and kinetic profiles with equilibria

Once an optimized ramp-down scenario is found, a consistent set of CHEASE equilibria can be calculated for time points along the optimized trajectory. This way, one can validate whether the impact of the optimized κ trace on the plasma state evolution has been correctly captured by the interpolation scheme to update the metrics **g** introduced in equation (7).

An automated function allows the user to provide the time points for which a consistent equilibrium is desired. For these times, equilibria are calculated with consistent q_{95}, elongation κ and kinetic profiles (p' and TT' consistent with the pressure p and current density j_{par} of the optimized RAPTOR simulation are provided to CHEASE). To prepare a LCFS contour with the desired value κ_{opt} for CHEASE, a set of plasma boundary control points $(R_{opt,i}, Z_{opt,i})$ are defined. These control points are calculated by selecting the LCFS contour (R_i, Z_i) of the equilibrium from the original sequence with elongation κ closest to the desired value κ_{opt} and by subsequently rescaling the vertical distance to the (SND) X-point for each control point: $(R_{opt,i}, Z_{opt,i}) = (R_i, Z_X + \frac{\kappa_{opt}}{\kappa}[Z_i - Z_X])$.

The initial sequence of CREATE-NL equilibria and a sequence of equilibria along an optimized ramp-down trajectory are indicated by sets of diamond symbols in figure 13. The boundary shape for an equilibrium at $t = 55\,\mathrm{s}$ (identified by the green boxes in the I_p and κ time trace plots) is compared between the original equilibrium (blue solid line) and the updated, consistent equilibrium (red dash-dotted line).

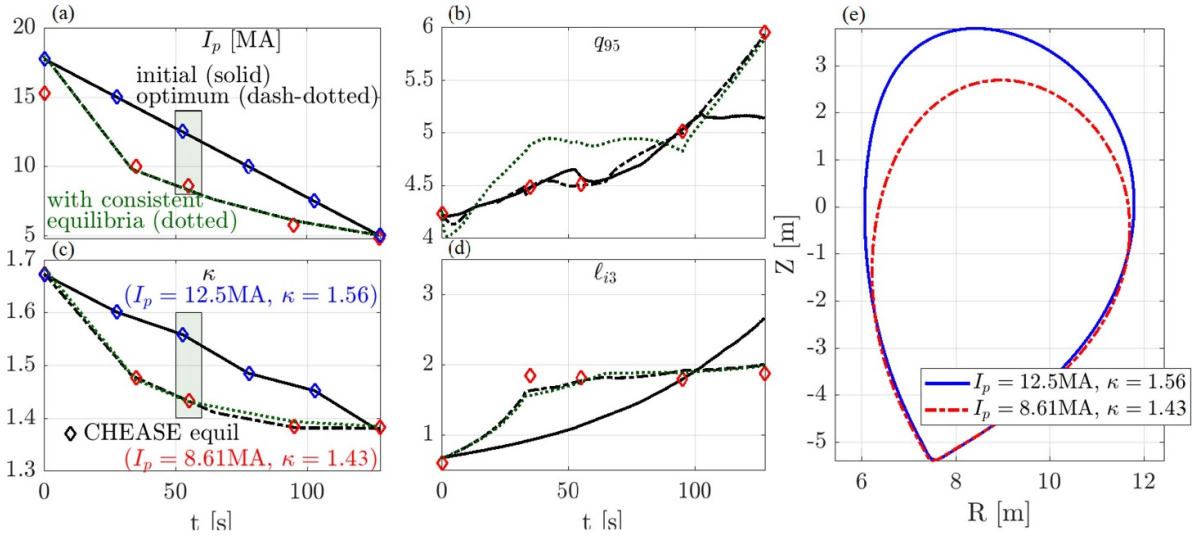

Figure 13. Initial and optimized time traces are shown for I_p, κ, q_{95} and ℓ_{i3} (for the case with $dI_p/dt = -100\,\mathrm{kA\,s^{-1}}$, late HL transition, hot L-mode in figure 11). The values of plasma current and elongation of the equilibria initially obtained from CREATE-NL are indicated by the blue diamonds. The red diamond symbols indicate the equilibria calculated during post-processing of the optimized results. These equilibria are calculated with values of q_{95}, κ and kinetic profiles consistent with the optimal trajectory. For an equilibrium at $t = 55\,\mathrm{s}$ (identified by the green boxes): the initial equilibrium boundary shape obtained from CREATE-NL is compared to the boundary shape with optimized κ. (a) $I_p(t)$; (b) $q_{95}(t)$; (c) elongation $\kappa(t)$; (d) ℓ_{i3}; (e) plasma boundary shape.

Now that a set of consistent equilibria has been calculated, we can verify whether the simplified treatment of equilibrium adjustments in the optimization scheme can be justified. Let us compare the ℓ_{i3} and q_{95} traces obtained with the optimizer (applying a simple, linear interpolation technique to evaluate **g**) with the respective values obtained with a RAPTOR simulation using the fully consistent CHEASE results as underlying equilibria. For ℓ_{i3} the changes are modest, justifying the applied linear interpolation procedure. For the q_{95} trace, the change between the optimized RAPTOR simulation without (black dash-dotted) and with consistent equilibria (green dotted) is more significant. The assessment of MHD stability of the proposed ramp-down trajectory requires more in-depth analysis, left for future work.

8. Summary of the main findings for DEMO ramp-down optimization

Let us summarize the main findings we can extract from the optimization of the diverted phase of the DEMO ramp-down in this paper, and from the insights gained in Part A [13]:

Reducing the plasma current ramp-rate $|dI_p/dt|$

- (+) slows down the increase of ℓ_{i3}, increasing the vertical stability margin (this effect is more efficient in conjunction with reducing the plasma cross-section);
- (+) reduces the magnitude of negative edge currents, which is in general safer with respect to ideal MHD stability;
- (+) increases the margin with respect to the Greenwald limit, relaxing density decay requirements;
- (+) unlike AUG observations, the poloidal flux swing for DEMO is little affected by changes in the length of the ramp-down time window and recharging is observed for all considered cases;
- (−) prolongs the ramp-down duration and the dwell time at high I_p.

Delaying the HL transition

- may be necessary if the fusion power cannot be reduced sufficiently rapid;
- (+) reduces flux consumption (more recharging), although the difference becomes smaller for faster ramp-down rates;
- (−) demands solutions for density decay and impurity control (fueling, ELM control …);
- (−) demands a significant amount of installed auxiliary power, to maintain a sufficient P_{sep} as P_{alpha} reduces;
- (−) prolongs the dwell time at high W_{th}.

Maintaining L-mode heating

- (+) helps maintaining a positive power balance, increasing the radiative collapse margin after the HL transition;
- (+) increases the density limit margin;
- (+) reduces the drop of β_{pol} during the HL transition, easing radial position control;
- (−) while a sudden increase of ℓ_{i3} is averted by maintaining heating for AUG L-modes, the highly transient current diffusion dynamics in the DEMO ramp-down show a dominant impact of the loop voltage profile shape rather than the $T_e^{3/2}$ profile; as increased temperatures lead to a larger resistive time τ_R, slowing down the current diffusion, larger values of ℓ_{i3} and a larger magnitude of negative edge currents result, reducing the vertical stability margin;
- (−) the reduction of separatrix power needs to be sufficiently significant to trigger the HL transition (considering the effective heating from $-dW_{th}/dt$), to be managed by real-time control.

Reducing the plasma cross-section (reducing the elongation κ)

- (+) slows down the increase of ℓ_{i3}, increasing the vertical stability margin (this effect is more efficient in conjunction with reducing $|dI_p/dt|$);
- (+) reduces the vertical instability growth rate by reducing the elongation, increasing the vertical stability margin;
- (−) reduces q_{95}, reducing the MHD stability margin;
- should maintain the magnetic geometry in the strike point region unchanged, as well as the shape in front of antennas if ion cyclotron (or lower hybrid) heating is being used.

Reduction of heavy impurity content of the plasma core

- (+) reduces the power radiated from the plasma core, increasing the radiative collapse margin;
- (−) increases conductivity and the resistive time τ_R, slowing down current diffusion, leading to larger values of ℓ_{i3}, reducing the vertical stability margin;
- (−) increases the separatrix power to be handled by the SOL.

9. Conclusion

The safe termination of burning plasmas is of crucial importance for the exploitation of DEMO, as very few disruption events can be tolerated (especially at plasma currents above $I_p \sim 5\,\mathrm{MA}$). The high radiated power fraction of DEMO, to limit the heat load to be handled by the divertor, will make the scenario sensitive to excursions from a nominal scenario, both in stationary state and during transient phases like ramp-down: a decrease of electron temperature leads to increasing average cooling factors for the intrinsic tungsten species and the seeded xenon species, potentially triggering a runaway process towards a radiative collapse. To avoid a radiative collapse during the ramp-down phase, significant plasma heating needs to be maintained during the L-mode phase (with the level of heating depending on how efficiently impurities can be removed from the plasma).

The present paper applies the gradient-based transport model introduced in [1]. A stationary RAPTOR reference for the DEMO stationary operating point is established, based on operating conditions discussed in the literature [8, 14, 40]. The simulation includes the effect of plasma dilution by the fusion-born helium species as well the radiation from tungsten and xenon, making use of ADAS cooling factor data [37]. A reactor operating point has been presented, considering the active constraints on performance, as well as physics limits. Importantly, a DEMO plasma is characterized by a high degree of self-regulation of the kinetic profiles (posing a challenge for kinetic profile control): the power balance is dominated by the plasma self-heating by the alpha fast particles, dependent on temperature and density profiles and fuel dilution, and the radiated power from heavy impurities, with a non-linear dependence on T_e.

The stationary operating point is used as initial condition for a series of ramp-down simulations. The technical and physical constraints that need to be simultaneously satisfied throughout the entire ramp-down phase raise a set of trade-offs when setting the actuator time traces. Leveraging the fast run time of the code, feasible DEMO ramp-down scenarios are developed in RAPTOR. A quantitative estimate is presented of the significant auxiliary heating required throughout the ramp-down phase, to avoid a radiative collapse.

Fast ramp-down scenarios are critical for emergency shutdown of the burning plasma, e.g. in case of divertor reattachment [14], and are actively analysed on present-day machines, e.g. after large tearing modes [2]. Ramping down the plasma current tends to cause a peaking of the current density profile, with a faster plasma current ramp-down rate leading to more significant peaking. In our simulations, significant peaking of j_{par} with inversion of the plasma current direction near the plasma edge is routinely observed. The corresponding increase of the plasma internal inductance ℓ_{i3} poses a challenge for the vertical position controllability of the plasma column, as thoroughly assessed in this paper. The MHD stability of these current density profiles should be assessed in future work.

An upper limit on the internal inductance from CREATE-NL [19] free boundary equilibrium control calculations is introduced [20], dependent on plasma current I_p and elongation κ. The feasibility of different plasma current ramp-down rates with respect to this vertical control limit is assessed: while a ramp-rate of $dI_p/dt = -50\,\mathrm{kA\,s^{-1}}$ (with ramp-down duration $t_{\mathrm{final}} = 256\,\mathrm{s}$) seems conservative, ramp-rates faster than $dI_p/dt = -100\,\mathrm{kA\,s^{-1}}$ ($t_{\mathrm{final}} = 128\,\mathrm{s}$) require active optimization. For a given ramp-rate, the increase of ℓ_{i3} can be limited by enhancing the outward diffusion of the current density: a lower temperature (lower L-mode confinement) or an increased effective charge Z_{eff} allows for a faster current diffusion time scale. The time traces of the plasma current $I_p(t)$ and the plasma elongation $\kappa(t)$ provide effective actuators to tailor the internal inductance trace $\ell_{i3}(t)$, allowing furthermore to reduce the maximum ℓ_{i3} without extending the time window used for the ramp-down. A reduction of the plasma elongation allows to enhance the vertical controllability of the plasma column, while a faster compression of the plasma results in a reduced increase of ℓ_{i3} according to RAPTOR modeling. Furthermore, during fast shape changes, a significant impact of $\dot{\Phi}_b$ (time derivative of the toroidal flux enclosed by the LCFS) on current density peaking has been identified. However, while reducing the plasma elongation, q_{95} should be maintained sufficiently high, by constraining how fast the plasma shape can be changed.

Applying the RAPTOR automated optimization routines introduced in [1], a set of feasible ramp-down trajectories has been derived, respecting dual constraints: while the internal inductance ℓ_{i3} is limited below the upper limit from CREATE-NL, a monotonic increase of q_{95} during the early ramp-down is forced. Imposing $\ell_{i3} < f_{\mathrm{margin}}\ell_{i3\ \mathrm{CREATE}}(I_p)$ with $f_{\mathrm{margin}} = 1.15$, a feasible ramp-down strategy could be found for an average ramp-down rate of $dI_p/dt = -100\,\mathrm{kA\,s^{-1}}$ ($t_{\mathrm{final}} = 128\,\mathrm{s}$), even for conservative assumptions regarding the HL transition and confinement quality (for $dI_p/dt = -150\,\mathrm{kA\,s^{-1}}$, $t_{\mathrm{final}} = 85\,\mathrm{s}$, a feasible ramp-down with $f_{\mathrm{margin}} = 1.15$ could

only be found under favorable confinement conditions: an early HL transition and low confinement quality during L mode allowing for faster outward current diffusion). For $dI_p/dt = -200\,\mathrm{kA\,s^{-1}}$ ($t_{\mathrm{final}} = 64\,\mathrm{s}$), a feasible ramp-down scenario could be found under favourable confinement conditions and assuming a larger margin $f_{\mathrm{margin}} = 1.30$ with respect to the constraint from CREATE-NL can be achieved. Note that the avoidance of negative current densities near the plasma edge has not been included as an objective in these optimizations. While geometry modifications between iterations of the optimizer have been implemented in an ad-hoc way, this approach has been successfully validated by re-simulating the optimized trajectories with a loose coupling to the CHEASE fixed boundary equilibrium solver.

The inherently coupled nature of the kinetic (q, T_e, n_e) and magnetic (position and shape) control problems demands integrated simulations to test the feasibility of established ramp-down strategies. The kinetic profile evolution of the optimum ramp-down trajectory should be confirmed with higher fidelity integrated modeling tools (including impurity transport, pedestal model etc). Ideally, whole-device modeling should be envisioned, including SOL dynamics and pumping efficiency. Iteration or coupling between a transport solver and a free boundary equilibrium control model (like CREATE-NL [19]) is required to assess controllability. More specifically: for the optimized ramp-down trajectories proposed in this paper, it should be verified whether the poloidal field coils allow for the proposed changes in plasma elongation, and whether the plasma equilibria can be maintained radially and vertically stable (for the modeled kinetic profile evolution, plasma elongation and for a given DEMO design, e.g. with or without in-vessel coils).

It should be emphasized that the optimized trajectory can be tailored in real-time with accurate knowledge, since RAPTOR is RT-compatible on present-day tokamaks and much more time and computing power is available in a DEMO reactor. In particular the best timing for the H-L transition can be determined under several pre-defined conditions, including the Greenwald fraction time evolution, and triggered in real-time when approaching an unsafe operating boundary. Similarly, the level of heating in L-mode should be as low as possible, while controlling the adequate power balance with respect to the radiated power.

Data availability statement

The data cannot be made publicly available upon publication because the cost of preparing, depositing and hosting the data would be prohibitive within the terms of this research project. The data that support the findings of this study are available upon reasonable request from the authors.

Acknowledgments

This work has been carried out within the framework of the EUROfusion Consortium, partially funded by the European Union via the Euratom Research and Training Programme (Grant Agreement No 101052200 - EUROfusion). The Swiss contribution to this work has been funded by the Swiss State Secretariat for Education, Research and Innovation (SERI). Views and opinions expressed are however those of the author(s) only and do not necessarily reflect those of the European Union, the European Commission or SERI. Neither the European Union nor the European Commission nor SERI can be held responsible for them. This work was supported in part by the Swiss National Science Foundation.

Appendix. Evaluating τ_E and $\tau_{E\ scl}$ in a plasma with high levels of radiated power

When evaluating the confinement enhancement factor $H = \tau_E/\tau_{E\ scl}$, a proper definition of the loss power P_L is required, present both in the confinement time formula $\tau_E = W_{th}/P_L$, and in the scaling law dependency $\tau_{E\ scl} = \tau_{E\ 98y,2} \sim P_L^{-0.69}$. The standard implementation of the gradient-based transport model assumes $P_L = P_{heat} - \dot{W}_{th}$, with P_{heat} the total plasma heating power (ohmic, alpha and auxiliary) and $\dot{W}_{th} = dW_{th}/dt$ (this term is equal to zero for the stationary operating points shown in this appendix, but non-zero during ramp-down). This definition of the loss power does not subtract any fraction of the power radiated directly from the core plasma. In [57], IPB98(y, 2) confinement scaling predictions are compared to ASTRA-TGLF simulations to come up with a proper P_L correction term accounting for the core radiated power. By subtracting 60% of the radiated power inside $\rho = 0.75$, the best agreement between simulation and scaling law is obtained, i.e. $P_L = P_{heat} - \dot{W}_{th} - P_{rad\ core}$ with $P_{rad\ core} = 0.6 \int_{\rho=0}^{0.75} p_{rad} dV$.

Applying these corrections in the gradient-based model impacts the predicted temperatures and stored thermal energies. For a given H factor, e.g. equal to unity, one can write $\tau_E = W_{th}/P_L \sim \tau_{E\ scl} = \tau_{E\ 98y,2} \sim P_L^{-0.69}$, hence for the resulting stored energy one can write $W_{th} \sim (P_L)_{\tau_E}(P_L)_{\tau_{E\ scl}}^{-0.69}$. While applying the $P_{rad\ core}$ subtraction in $(P_L)_{\tau_E}$ leads to a reduced W_{th}, the loss power correction in the scaling law tends to increase W_{th} (since confinement degrades with increasing power). Depending on which of both loss power factors $(P_L)_{\tau_E}$ and $(P_L)_{\tau_{E\ scl}}$ is corrected with a radiated power subtraction, we can hence distinguish four cases[13] (the three cases for which a RAPTOR stationary state is found are shown in figure A1 and table A1):

- The electron temperature profile for the reference case without loss power corrections is represented in blue in figure A1.
- The net effect of the double loss power correction proposed in [57] leads to a reduced W_{th}. This can be illustrated by comparing the blue and the dashed red T_e profiles in figure A1.

[13] While $(P_L)_{\tau_E} = (P_L)_{\tau_{E\ scl}}$ is the most consistent assumption [57], we include all four cases to provide a more complete overview of the impact of the different definitions on the predicted temperature and stored thermal energy.

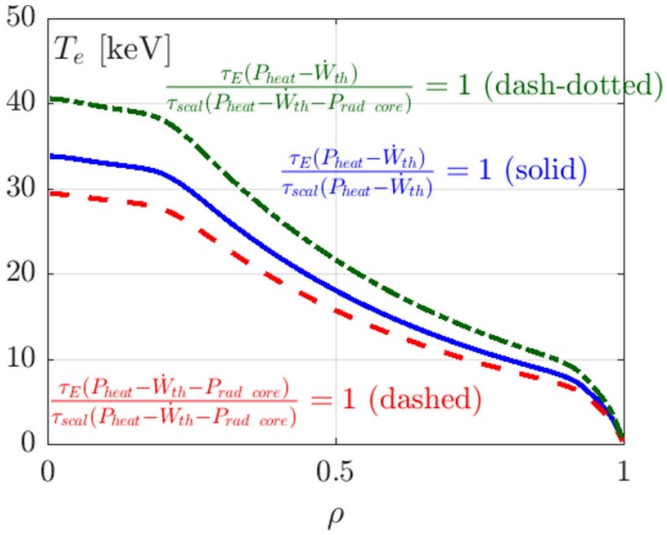

Figure A1. A comparison is shown between T_e profiles for the DEMO stationary state calculated in RAPTOR, for different assumptions regarding the way radiated power is taken into account when calculating the loss power. The three profiles have an H factor equal to unity $H_{98y,2} \sim (P_L)^{0.69}_{\tau_{E\ scl}} W_{th}/(P_L)_{\tau_E} = 1$. For the blue profile $(P_L)_{\tau_E} = (P_L)_{\tau_{E\ scl}} = P_{heat} - \dot{W}_{th}$, corresponding to the standard implementation of the gradient-based model as applied in this paper. For the red dashed profile $(P_L)_{\tau_E} = (P_L)_{\tau_{E\ scl}} = P_{heat} - \dot{W}_{th} - P_{rad\ core}$, as proposed in [57]. For the green dash-dotted profile, $(P_L)_{\tau_{E\ scl}} = P_{heat} - \dot{W}_{th} - P_{rad\ core}$, while $(P_L)_{\tau_E} = P_{heat} - \dot{W}_{th}$.

Table A1. The stationary DEMO operating points obtained in RAPTOR are presented, for different assumptions regarding the way radiated power is taken into account when calculating the loss power. The three cases have an H factor equal to unity $H_{98y,2} = (P_L)^{0.69}_{\tau_{E\ scl}} W_{th}/(P_L)_{\tau_E} = 1$. The first two columns indicate whether or not $P_{rad\ core}$ is subtracted, respectively in the loss power terms $(P_L)_{\tau_E}$ and $(P_L)_{\tau_{E\ scl}}$.

$(P_L)_{\tau_E}$	$(P_L)_{\tau_{E\ scl}}$	$H_{98y,2}$ (no $P_{rad\ core}$)	$P_{rad\ core}$	W_{th}
~~$-P_{rad\ core}$~~	~~$-P_{rad\ core}$~~	1.01	102 MW	1257 MJ
$-P_{rad\ core}$	$-P_{rad\ core}$	0.92	105 MW	1093 MJ
~~$-P_{rad\ core}$~~	$-P_{rad\ core}$	1.15	102 MW	1508 MJ

- Subtracting $P_{rad\ core}$ only in the scaling law evaluation would lead to the dash-dotted green profile in figure A1, with improved confinement.
- No stationary operating point was found for the case where $P_{rad\ core}$ is only subtracted for the confinement time evaluation. This can be understood by considering the corresponding expression:

$$H_{98y,2} = \frac{\tau_E}{\tau_{E\ 98y,2}} \sim \frac{W_{th}}{P_{heat} - \dot{W}_{th} - P_{rad\ core}} \left(P_{heat} - \dot{W}_{th}\right)^{0.69} \tag{A.1}$$

  Evaluating this expression with the T_e profile obtained with the standard settings of the gradient-based model (no $P_{rad\ core}$ subtraction, blue profile in figure A1), leads to an H factor above one (confinement is degraded, the blue T_e is too optimistic). However, by decreasing T_e, both numerator and denominator decrease, respectively due to a reduced W_{th} and an increased $P_{rad\ core}$. Interestingly, this leads to the fact that, when reducing T_e (by reducing μ_{T_e}), no profile satisfying $H_{98y,2} = 1$ is found.

In this paper, the H factor is calculated without subtracting $P_{rad\ core}$ in $(P_L)_{\tau_E}$ and $(P_L)_{\tau_{E\ scl}}$. Not applying the $P_{rad\ core}$ corrections as proposed in [57] in the gradient-based transport model is equivalent to assuming a confinement enhancement of about 10%.

ORCID iDs

S Van Mulders https://orcid.org/0000-0003-3184-3361
O Sauter https://orcid.org/0000-0002-0099-6675
E Fable https://orcid.org/0000-0001-5019-9685
F Felici https://orcid.org/0000-0001-7585-376X
M Mattei https://orcid.org/0000-0001-7951-6584
F Palermo https://orcid.org/0000-0002-7524-3248
A A Teplukhina https://orcid.org/0000-0002-9213-7594

References

[1] Teplukhina A A, Sauter O, Felici F, Merle A and Kim D (TCV Team, ASDEX Upgrade Team and EUROfusion MST1 Team)
2017 Simulation of profile evolution from ramp-up to ramp-down and optimization of tokamak plasma termination with the RAPTOR code *Plasma Phys. Control. Fusion* **59** 124004

[2] Barr J L *et al* (DIII-D Team) 2021 Development and experimental qualification of novel disruption prevention techniques on DIII-D *Nucl. Fusion* **61** 126019

[3] Fable E *et al* (ASDEX Upgrade Team) 2013 Novel free-boundary equilibrium and transport solver with theory-based models and its validation against ASDEX Upgrade current ramp scenarios *Plasma Phys. Control. Fusion* **55** 124028

[4] Fietz S, Fable E, Hobirk J, Fischer R, Fuchs C, Pereverzev G and Ryter F (ASDEX Upgrade Team) 2013 Investigation of transport models in ASDEX Upgrade current ramps *Nucl. Fusion* **53** 053004

[5] Bizarro J P S , Köchl F and Voitsekhovitch I (JET EFDA Contributors) 2016 Modelling the ohmic l-mode ramp-down phase of JET hybrid pulses using JETTO with Bohm-Gyro-Bohm transport *Plasma Phys. Control. Fusion* **58** 105010

[6] de La Luna E, Loarte A, Rimini F, de Vries P, Koechl F, Reux C, Lomas P, Buratti P and Carvalho P 2018 Impact of ELM control in JET experiments on H-mode terminations with/without current ramp-down and implications for ITER *Proc. 27th IAEA Fusion Energy Conf., IAEA (Vienna)* pp 2–1

[7] Koechl F *et al* (JET Contributors) 2018 W transport and accumulation control in the termination phase of JET H-mode discharges and implications for ITER *Plasma Phys. Control. Fusion* **60** 074008

[8] Giruzzi G *et al* 2015 Modelling of pulsed and steady-state DEMO scenarios *Nucl. Fusion* **55** 073002

[9] Artaud J F *et al* 2018 METIS: a fast integrated tokamak modelling tool for scenario design *Nucl. Fusion* **58** 105001

[10] Poli F M, Kim S H, de Vries P C, Gribov Y, Polevoi A, Koechl F and Kavin A 2018 The plasma current ramp-down in ITER: physics constraints on control *27th IAEA Fusion Energy Conf.*

[11] de Vries P C *et al* 2018 Multi-machine analysis of termination scenarios with comparison to simulations of controlled shutdown of ITER discharges *Nucl. Fusion* **58** 026019

[12] Loarte A *et al* 2016 Evaluation of tungsten transport and concentration control in ITER scenarios *26th 2016 IAEA Fusion Energy Conf.*

[13] Van Mulders S, Sauter O, Contré C, Felici F, Fischer R, Pütterich T, Sieglin B and Teplukhina A A (ASDEX Upgrade Team) 2023 Scenario optimization for the tokamak ramp-down phase in RAPTOR. Part A: analysis and model validation on ASDEX Upgrade *Plasma Phys. Control. Fusion* **66** 025006

[14] Siccinio M *et al* 2020 Demo physics challenges beyond ITER *Fusion Eng. Des.* **156** 111603

[15] Ostuni V *et al* (WEST Team) 2022 Core radiative collapse characterisation and integrated modelling in west plasmas *Nucl. Fusion* **62** 106034

[16] Maviglia F *et al* 2021 Impact of plasma-wall interaction and exhaust on the EU-DEMO design *Nucl. Mater. Energy* **26** 100897

[17] Siccinio M, Federici G, Kembleton R, Lux H, Maviglia F and Morris J 2019 Figure of merit for divertor protection in the preliminary design of the EU-DEMO reactor *Nucl. Fusion* **59** 106026

[18] Del Nevo A 2018 Direct coupling of WCLL BB PHTS to PCS feasibility study - preliminary PCS design with an internal source of energy to operate at a minimum load the steam turbine and the power cycle in dwell *Eurofusion*

[19] Albanese R, Ambrosino R and Mattei M 2015 Create-NL+: a robust control-oriented free boundary dynamic plasma equilibrium solver *Fusion Eng. Des.* **96–97** 664–7

[20] Mattei M, Albanese R and Ambrosino R 2016 Final Report on Deliverable PMI-5.2.1-T010-D001 Scenario Modelling *Eurofusion*

[21] Federici G *et al* 2019 Overview of the DEMO staged design approach in Europe *Nucl. Fusion* **59** 066013

[22] Greenwald M, Terry J L, Wolfe S M, Ejima S, Bell M G, Kaye S M and Neilson G H 1988 A new look at density limits in tokamaks *Nucl. Fusion* **28** 2199–207

[23] Lang P T *et al* (ASDEX Upgrade Team) 2012 High-density h-mode operation by pellet injection and ELM mitigation with the new active in-vessel saddle coils in ASDEX Upgrade *Nucl. Fusion* **52** 023017

[24] Giacomin M, Pau A, Ricci P, Sauter O and Eich T (JET Contributors and ASDEX Upgrade Team) 2022 First-principles density limit scaling in tokamaks based on edge turbulent transport and implications for ITER *Phys. Rev. Lett.* **128** 185003

[25] Politzer P A, Jackson G L, Humphreys D A, Luce T C, Hyatt A W and Leuer J A 2010 Experimental simulation of ITER rampdown in DIII-D *Nucl. Fusion* **50** 035011

[26] Van Mulders S, Felici F, Sauter O, Citrin J, Ho A, Marin M and van de Plassche K L 2021 Rapid optimization of stationary tokamak plasmas in RAPTOR: demonstration for the ITER hybrid scenario with neural network surrogate transport model QLKNN *Nucl. Fusion* **61** 086019

[27] Weiland M, Bilato R, Dux R, Geiger B, Lebschy A, Felici F, Fischer R, Rittich D and van Zeeland M (ASDEX Upgrade Team) 2018 RABBIT: real-time simulation of the NBI fast-ion distribution *Nucl. Fusion* **58** 082032

[28] van Dongen J, Felici F, Hogeweij G M D, Geelen P and Maljaars E 2014 Numerical optimization of actuator trajectories for ITER hybrid scenario profile evolution *Plasma Phys. Control. Fusion* **56** 125008

[29] Wesson J 2004 *Tokamaks* 3rd edn (Oxford Science Publications)

[30] Siccinio M *et al* 2018 Development of a plasma scenario for the EU-DEMO: current activities and perspectives *Proc. of the 2018 IAEA Fusion Energy Conf. (Gandhinagar, India, 22 October–27 October 2018)*

[31] Kumar N, Camenen Y, Benkadda S, Bourdelle C, Loarte A, Polevoi A R and Widmer F (JET Contributors) 2020 Turbulent transport driven by kinetic ballooning modes in the inner core of JET hybrid H-modes *Nucl. Fusion* **61** 036005

[32] Van Mulders S 2023 Full-discharge simulation and optimization with the RAPTOR code, from present tokamaks to ITER and DEMO *PhD Thesis* École Polytechnique Fédérale de Lausanne (EPFL)

[33] ITER Physics Expert Group on Confinement and Transport, ITER Physics Expert Group on Confinement Modelling and Database and ITER Physics Basis editors 1999 Chapter 2: plasma confinement and transport *Nucl. Fusion* **39** 2175–249

[34] Polevoi A R *et al* 2015 Assessment of operational space for long-pulse scenarios in ITER *Nucl. Fusion* **55** 063019

[35] Van Mulders S, Sauter O, Bock A, Burckhart A, Contré C, Felici F, Fischer R, Schramm R, Stober J and Zohm H (ASDEX Upgrade Team) 2023 Inter-discharge optimization for fast, reliable access to ASDEX Upgrade AT scenario *Nucl. Fusion* accepted

[36] Fajardo D, Angioni C, Casson F J, Robert Field A, Maget P and Manas P (ASDEX Upgrade Team and JET Contributors) 2023 Analytical model for the combined effects of rotation and collisionality on neoclassical impurity transport *Plasma Phys. Control. Fusion* **65** 035021

[37] Atomic data and analysis structure (ADAS) (available at: www.adas.ac.uk/)

[38] Maget P *et al* (WEST Team) 2022 Healing plasma current ramp-up by nitrogen seeding in the full tungsten environment of WEST *Plasma Phys. Control. Fusion* **64** 045016

[39] Felici F, Citrin J, Teplukhina A A, Redondo J, Bourdelle C, Imbeaux F and Sauter O (JET Contributors and

EUROfusion MST1 Team) 2018 Real-time-capable prediction of temperature and density profiles in a tokamak using RAPTOR and a first-principle-based transport model *Nucl. Fusion* **58** 096006
[40] Zohm H *et al* 2013 On the physics guidelines for a tokamak DEMO *Nucl. Fusion* **53** 073019
[41] Stober J *et al* 2015 High power ECRH and ECCD in moderately collisional ASDEX Upgrade Hmodes and status of EC system upgrade *EPJ Web of Conferences* vol 87 p 02004
[42] Fable E *et al* (ASDEX Upgrade Team) 2019 The role of the source versus the collisionality in predicting a reactor density profile as observed on ASDEX Upgrade discharges *Nucl. Fusion* **59** 076042
[43] Zagorski R, Ivanova-Stanik R I and Stankiewicz R 2013 Simulations with the COREDIV code of DEMO discharges *Nucl. Fusion* **53** 073030
[44] Becker G 1988 Empirical scaling laws for local transport in neutral beam heated plasmas *Nucl. Fusion* **28** 1458
[45] Martin Y R and Takizuka T (ITPA CDBM H-mode Threshold Database Working Group) 2008 Power requirement for accessing the H-mode in ITER *J. Phys.: Conf. Ser.* **123** 012033
[46] Sauter O, Angioni C and Lin-Liu Y R 1999 Neoclassical conductivity and bootstrap current formulas for general axisymmetric equilibria and arbitrary collisionality regime *Phys. Plasmas* **6** 2834–9
[47] Sauter O, Angioni C and Lin-Liu Y R 2002 Erratum: "neoclassical conductivity and bootstrap current formulas for general axisymmetric equilibria and arbitrary collisionality regime" [phys. plasmas 6, 2834 (1999)] *Phys. Plasmas* **9** 5140
[48] Romero J A (JET-EFDA Contributors) 2010 Plasma internal inductance dynamics in a tokamak *Nucl. Fusion* **50** 115002
[49] Piron C *et al* 2015 Real-time simulation of internal profiles in the presence of sawteeth using the raptor code and applications to ASDEX Upgrade and EFX-mod *Europhysics Conf. Abstracts* vol 39E p 1.145
[50] Porcelli F, Boucher D and Rosenbluth M N 1996 Model for the sawtooth period and amplitude *Plasma Phys. Control. Fusion* **38** 2163
[51] Sauter O, Angioni C, Boucher D, Furno I, Pochelon A and Porcelli F 1998 Sawtooth period simulations of tcv discharges *Proc. Joint Varenna-Lausanne Int. Workshop on Theory of Fusion Plasmas (Varenna, Italy, August 1999)* pp 403–8
[52] Kim D, Goodman T P and Sauter O 2014 Real-time sawtooth control and neoclassical tearing mode preemption in ITER *Phys. Plasmas* **21** 061503
[53] Eriksson L-G *et al* 2004 Destabilization of fast-ion-induced long sawteeth by localized current drive in the JET tokamak *Phys. Rev. Lett.* **92** 235004
[54] Felici F and Sauter O 2012 Non-linear model-based optimization of actuator trajectories for tokamak plasma profile control *Plasma Phys. Control. Fusion* **54** 025002
[55] Teplukhina A 2018 Realistic multi-machine tokamak profile simulations and numerical ramp-down optimization using the RAPTOR code *PhD Thesis* École Polytechnique Fédérale de Lausanne (EPFL)
[56] Nocedal J and Wright S J 2006 *Numerical Optimization* 2nd edn (Springer)
[57] Lux H, Kemp R, Fable E and Wenninger R 2016 Radiation and confinement in 0D fusion systems codes *Plasma Phys. Control. Fusion* **58** 075001